5-2017

# Linear Quadratic Optimal Control for a Cascaded Converters-Based Microgrid

Amlam Niragire
*University of Arkansas, Fayetteville*

Linear Quadratic Optimal Control for a Cascaded Converters-Based Microgrid

A thesis submitted in partial fulfillment
of the requirements for the degree of
Master of Science in Electrical Engineering

by

Amlam Niragire
Harding University
Bachelor of Science in Electrical Engineering, 2014

May 2017
University of Arkansas

This thesis is approved for recommendation to the Graduate Council.

_____
Dr. Roy A. McCann
Thesis Director

_____
Dr. Juan C. Balda
Committee Member

_____
Dr. Yue Zhao
Committee Member

**ABSTRACT**

There is a constant transformation of the electric grid due to an ongoing interest in the deployment of renewable energy resources and electric microgrid formation. This transformation, though advantageous in many ways, poses great challenges for the energy industry and there must be a constant improvement in modeling, simulation, analysis and control techniques in order to characterize and optimize the system design and operation. In this light, the scope of this thesis is focused on developing a linear model, analyzing the stability and designing an optimal linear quadratic regulator (LQR) for a microgrid system. The microgrid system used is inspired by an existing, operational grid-connected microgrid testbed at the National Center for Reliable Electric Power Transmission (NCREPT). Simulation results using Matlab/Simulink™ show that the linearized model has the same dynamics and converges to the same steady state values as the actual model with minimal error. The simulation results also show that the system's stability margin lessens as the input impedance to the microgrid increases; suggesting a weaker coupling. Finally, it is observed through simulation that the proposed LQR controller remarkably improves the voltage settling time and overshoot, henceforth ameliorating the ability to include larger renewable generation capacity.

**ACKNOWLEDGEMENTS**

I am very grateful to Dr. Roy A. McCann for his immense help in many aspects of this endeavor. He has offered me prodigious guidance. Likewise, I sincerely thank each one of my thesis committee members for their profound, insightful and constructive feedbacks.

I also extend my special thanks to my wife, my family and friends for their diversified support throughout my studies. I find it impeccable to acknowledge their contribution, and I am so grateful to them.

**TABLE OF CONTENTS**

**CHAPTER I INTRODUCTIONS ..... 1**

I.1 Distributed Generation and the Electric Power Grid of the Future ..... 1

I.2 Thesis Motivation ..... 3

I.3 Thesis Objective ..... 5

I.4 Approach ..... 6

I.5 Thesis Organization ..... 7

**CHAPTER II BACKGROUND ..... 8**

II.1 Introduction ..... 8

II.2 NCREPT Microgrid System Overview ..... 8

II.3 Direct-Quadrature-Zero (dq0) Transformation ..... 11

**CHAPTER III MICROGRID SYSTEM MODELING ..... 16**

III.1 Introduction ..... 16

III.2 Circuit Model ..... 17

III.3 Nonlinear Mathematical Model ..... 18

III.4 Model Linearization for Controller Development ..... 23

III.5 Linear Model Validation ..... 28

**CHAPTER IV SYSTEM POLE-BASED STABILITY ANALYSIS ..... 36**

IV.1 Introduction ..... 36

IV.2 A Weakly Connected Microgrid ..... 37

IV.3 Stability Analysis Method ..... 38

IV.4 Stability Analysis Implications and Potential Benefits ..... 40

**CHAPTER V LINEAR QUADRATIC OPTIMAL CONTROLLER DESIGN . 41**

V.1 Introduction ..... 41

V.2 Linear Quadratic Optimal Control ..... 41

V.3 Implementation in Matlab/Simulink™ ..... 44

**CHAPTER VI SIMULATION RESULTS AND ANALYSIS ..... 47**

VI.1 Introduction ..... 47

VI.2 The Controlled Systems and Output States Selection ..... 47

VI.3 Results ..... 49

VI.3 Results Analysis ..... 54

**CHAPTER VII CONCLUSIONS AND FUTURE WORK ..... 56**

VII.1 Introduction ..... 56

VII.2 Conclusions ..... 57

VII.3 Future Work ..... 58

**REFERENCES ..... 60**

**APPENDICES ..... 63**

Appendix A: NCREPT Microgrid System Parameters ..... 63

Appendix B: Sample Transfer Functions in the Laplace Domain ..... 65

Appendix C: Actual Model Measured States before Applying a Low Pass Filter ..... 66

Appendix D: Mathematical Model Measured States before Applying a Low Pass Filter ..... 68

Appendix E: Controller Performance Evaluation – Supplemental Data ..... 70

Appendix F: System Matrix for the Linearized Mathematical Model ..... 71

**TABLE OF FIGURES**

Fig. 1. AC grid-connected microgrid configuration. ..... 3

Fig. 2. AC microgrid dc bus voltage instability – VVVF drive. ..... 4

Fig. 3. AC microgrid dc bus voltage instability – regen drive. ..... 5

Fig. 4. NCREPT test facility building at the Arkansas engineering research center. ..... 8

Fig. 5. NCREPT one-line diagram. ..... 9

Fig. 6. NCREPT bay area. ..... 10

Fig. 7. Hybrid microgrid configuration. ..... 10

Fig. 8. Back-to-back topology for the Regen and the VVVF drives ..... 11

Fig. 9. Geometric relationship between ABC, αβ0, and dqo reference frames [12]. ..... 15

Fig. 10. Cascaded converters-based microgrid system. ..... 16

Fig. 11. Single phase equivalent circuit for network controller development. ..... 17

Fig. 12. Actual circuit model as modeled in Matlab/Simulink™. ..... 28

Fig. 13. Mathematical model. ..... 30

Fig.. 14. Mathematical model equations sample ..... 30

Fig. 15. Filtered inductor currents for the actual circuit model. ..... 31

Fig. 16. Filtered capacitor voltages for the actual circuit model. ..... 32

Fig. 17. Filtered inductor currents for the mathematical model. ..... 32

Fig. 18. Filtered capacitor voltages for the mathematical model. ..... 33

Fig. 19. Microgrid systems - input impedance. ..... 36

Fig. 20. Input impedance variation range. ..... 37

Fig. 21. Change in eigenvalues with variation of input impedance. ..... 38

Fig. 22. Change in eigenvalues with variation of input impedance (Cont.). ..... 39

Fig. 23. LQR for a system with all states available for measurement. ..... 42

Fig. 24. Implementation of an LQR with a Kalman filter. ..... 43

Fig. 25. Implementation of an LQR with a Kalman filter and integral of the error. ..... 44

Fig. 26. MIMO system representation of the microgrid system. ..... 45

Fig. 27. Arbitrary nodes used to states presented in this chapter. ..... 48

Fig. 28. Step response of dc-link voltages: VVVF (top) and regen drive (bottom). ..... 50

Fig. 29. Step response for load voltage at node 3: direct axis (top) and quadrature axis (bottom). ..... 51

Fig. 30. Step response for load voltage at node 4: direct axis (top) and quadrature axis (bottom). ..... 53

# CHAPTER I INTRODUCTIONS

## I.1 Distributed Generation and the Electric Power Grid of the Future

The electric power grid has seen a tremendous transformation since the discovery of electricity in the 18th century. From the discovery of the first transformer in the late 19th century to today's advanced technologies in measurement and sensors, Internet, communications, power electronics, and various types of control, the electric grid has emerged from a simple few-miles network to cross-country and cross-nation power grids. In [1], the authors propose a European mega-grid, which should be able to enable the region to profit from the diversity in energy supply and demand, and would facilitate the sharing of technologically and topographically uneven energy resources across the region.

Even with the above-mentioned developments, problems related to electric power quality are still of concern. There are several definitions of electric power quality in existence, but one commonly used defines it as a collection of parameters that sets forth the properties and qualities of ready-to-use power under normal conditions of operation in regards to the continuity of service and voltage characteristics such as frequency, symmetry, waveform and magnitude [2]. Any deviations from these normal conditions can cause considerable harm to sensitive loads: a minor power interruption can cause serious problems during a technology-based surgery operation, such as those commonly performed in hospitals. Likewise, critical information can be lost in data centers and servers, which require that power be continuously available for their operation. Other sensitive load examples include but are not limited to time-sensitive manufacturing facilities where companies can lose a considerable amount of money due to power outages. Many remedies exist for power quality related problems. These remedies include capacitor banks, voltage regulators,

uninterrupted power supplies (UPS's) … etc. Among these power quality solutions, distributed generation is considered to be especially significant to the scope of this thesis.

Also, utility companies and governments around the globe are concerned with serious energy issues. Two of these are most important: increased energy demand faced with shrinking energy resources, and the impact of these conventional energy resources on the environment. Consequently, the deployment of renewable resources at the distribution level has gained attention as a promising solution to the problems associated with fossil fuels and those of limited generation capacity expansion in face of the continuous rise in energy demand [3]. This has resulted in distributed generation systems forming microgrid, which play a crucial role in effective utilization of energy resources and can help stabilize the public power grid [4]. With the technology available today and research efforts across the globe, the megagrid of the type discussed in [1] is becoming a reality.

However, the current and future trends in electric power grid bring benefits and challenges alike. As the authors of [5] put it, the continuous penetration of sporadic renewable energy resources is introducing many operational and technical issues in different areas such as safety and protection, reliability and power quality, load management, grid interconnections and the required controls, and even in regulation of the electricity market. In fact, integrating distributed generators into the power grid introduces bidirectional power flow with the resulting system, which not only challenges its stability but also the traditional practices used in the metering and protection thereof [6]. Moreover, different topologies continue being proposed for interfacing microgrids with the national electric grid. The resulting network of interconnected power electronic converters can cause system power flow instability as discussed in [7]. The latter issue constitutes what this thesis mainly focuses on, as will be described in the following sections.

## I.2 Thesis Motivation

The concept of electric energy is simply fascinating. One could argue that it is the backbone of the modern economy. Indeed, it is impossible to imagine life today without electricity, and the need for it continues to grow more than ever. Research into this area is highly active around the world: especially in the quest to harvest renewable energy resources. This alone constitutes more than enough motivation for the work in this thesis, but the specific incentive is due to the microgrid instability case observed at NCREPT.

As discussed in the previous section, there is an ongoing integration of renewable resources into the lectric grid. The result is a system incorporating microgrids, which can operate in grid-connected or isolated mode or both. As such, an ac grid-connected microgrid exists at the University of Arkansas (covered in detail in Chapter two).

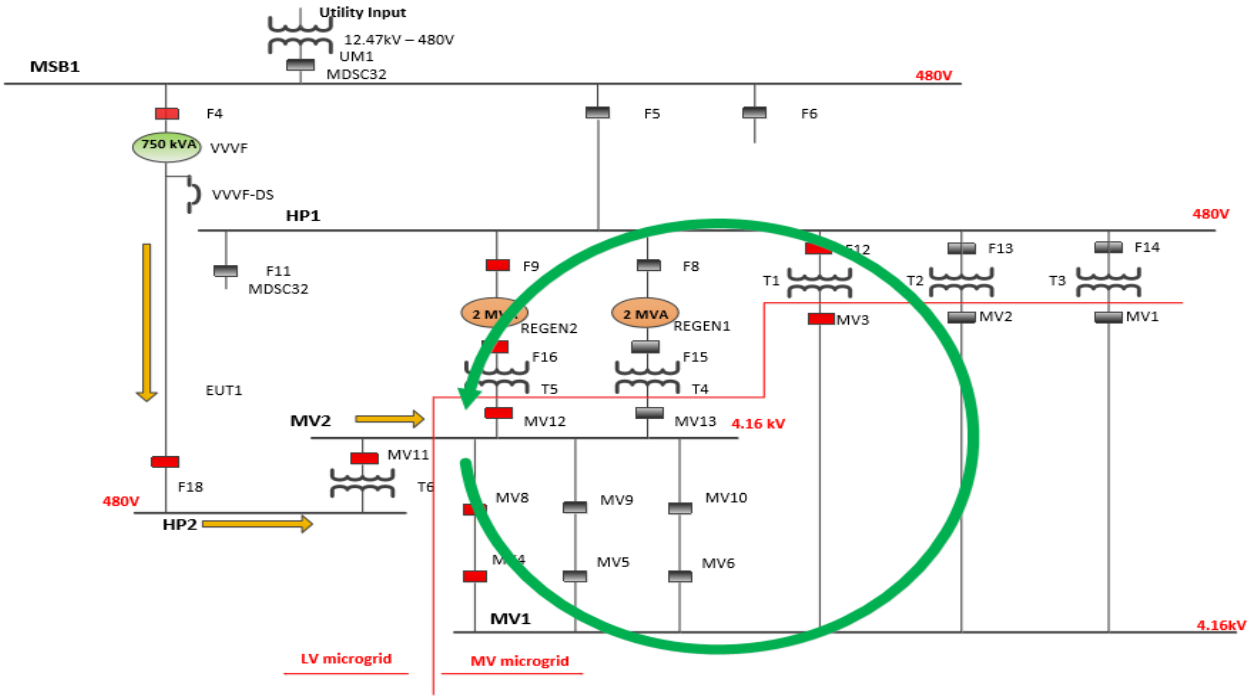


Fig. 1. AC grid-connected microgrid configuration [26].

During an experimental test, the microgrid configuration shown in Fig. 1 resulted in the following voltage instability case: there are two back-to-back converters in Fig. 1 named VVVF and Regen, and either one has a dc-link capacitor to store energy.

During the experiment, each dc-link capacitor was allowed to charge independently by energizing the sub-microgrid in which it was contained. In this operation, the controllers managed to keep the two systems stable. This is illustrated in about the first 75 seconds on both Fig. 2 and Fig. 3, where the dc bus voltages are kept constant by the action of the controllers. Nevertheless, when the final switch is thrown to make the circuit in Fig. 1, the system suddenly fails to maintain stability as shown in both Fig. 2 and Fig. 3. As a result, this thesis focuses on modeling, linearizing, analyzing, and designing a linear quadratic regulator for a microgrid of the same type as that in Fig. 1.

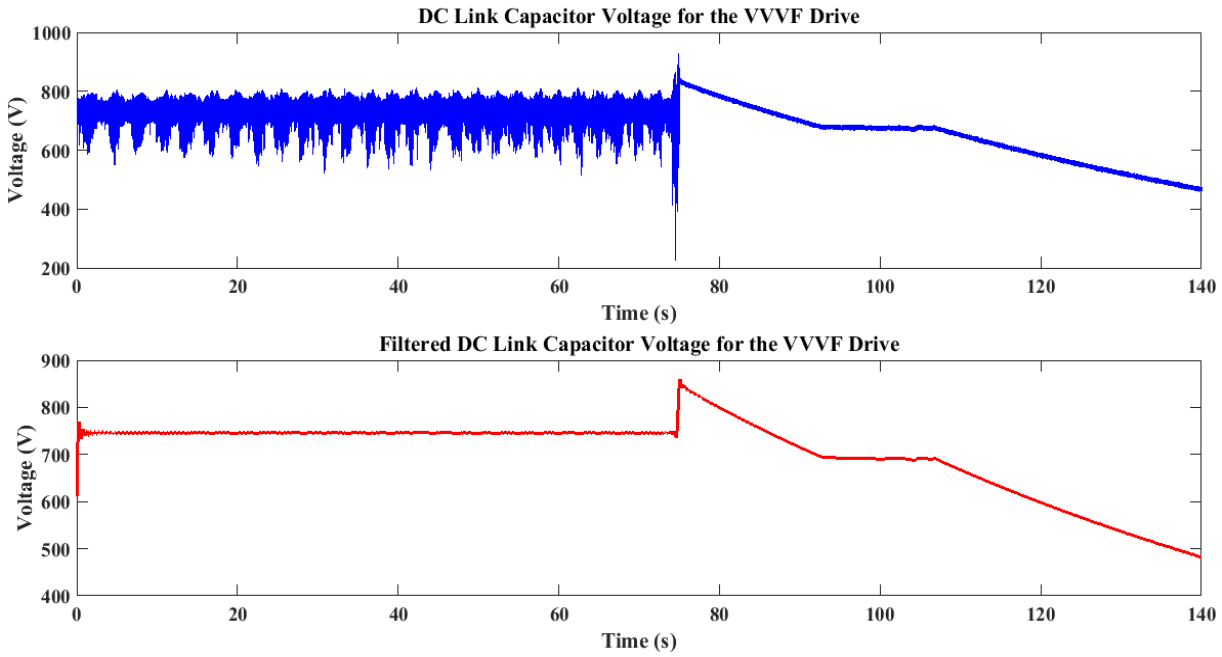


Fig. 2. AC microgrid dc bus voltage instability – VVVF drive.

## I.3 Thesis Objective

The main objective envisaged by this thesis consists of designing and simulating an advanced and robust control scheme–namely a linear quadratic regulator (LQR) optimal controller for a cascaded inverters-based microgrid system using state space method.

- ✓ Develop an accurate mathematical model, which represents a physical system and matches the simulation model. This ensures that the controller developed reflects the dynamics of the system and controls the realistic and accurate system model. The developed model can be used for other research initiatives and analyses.
- ✓ Perform a stability analysis of the system to determine some of the factors that can affect its stability margin. The impact of the variability of the input impedance on the system's stability is analyzed. This investigation is important in controller design.
- ✓ Design a linear quadratic optimal controller to improve the system's stability margin and analyze its performance in that regard.

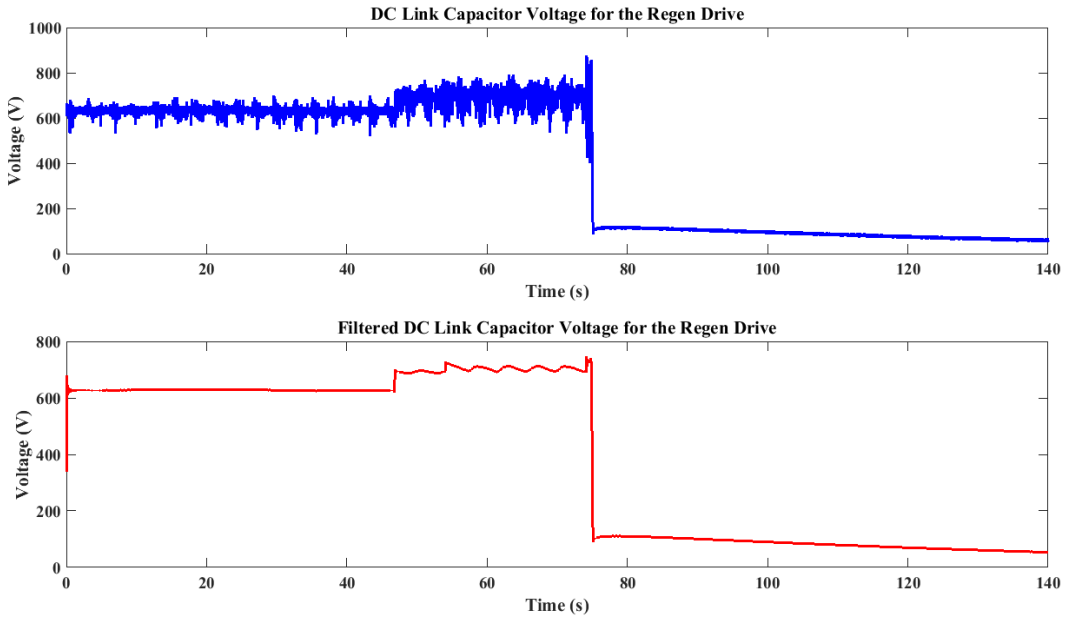


Fig. 3. AC microgrid dc bus voltage instability – regen drive.

It follows that the central point of this work is to propose a control scheme whose performance increases the stability margin of the microgrid system, which in return improves its power-rating capacity. The proposed control scheme is an optimal linear quadratic regulator, which is discussed in latter chapters. The microgrid system used is inspired by the 6 MVA microgrid testbed located at the NCREPT facility at the University of Arkansas Research and Technology Park [8].

## I.4 Approach

Matlab/Simulink™ software package was used extensively both for design and analysis throughout this work. A series of steps were followed in an effort to develop an accurate mathematical model. A representative microgrid system is designed based on the 6 MVA one at the NCREPT [8]. Assuming a balanced three-phase system, the per-phase circuit was used to derive a set of differential equations (DEs) governing the system, which are then transformed in the rotating d-q reference frame to facilitate the analysis. To validate the accuracy of the obtained mathematical model, Matlab/Simulink™ is used to compare the solutions to the obtained DEs and the simulation results of an actual circuit. After a series of checks and corrections, the two models finally converged to the same solution, henceforth proving the accuracy of the developed linear mathematical model.

To investigate the effect of the change in input impedance to the stability margin of the system, a poles-based analysis was performed. Using the model obtained in the previous step, the input impedance was varied, and the system's poles were plotted.

Finally, an LQG optimal controller was designed, and its performance evaluated in comparison to that of a conventional proportional plus integral (PI) control method.

## I.5 Thesis Organization

The rest of this work is structured in the following manner: Chapter II provides a brief description of the NCREPT microgrid system. It also covers others works related to the scope of this thesis and briefly introduces the rotating dq0 reference frame. Chapter III details how the mathematical model was developed and validated for accuracy assurance. In Chapter IV, the analysis of the developed system's stability is explored whereas in Chapter V the control development and design is presented. Chapter VI discusses the results and the analysis thereof, and Chapter VII states the conclusions, contributions and future work.

# CHAPTER II BACKGROUND

## II.1 Introduction

This chapter provides a brief description and background of the microgrid system at NCREPT. It introduces the microgrid concept in more detail and highlights different types of microgrids. In addition, a brief discuss of the direct-quadrature-zero (dq0) transformation is given. The final equations, which explicitly give the direct axis and quadrature axis components are derived for a balanced three phase system. The dq0 transformation is used in the chapter III to transform the alternating current (ac) states to direct current (dc), which simplifies the analysis and controller development.

## II.2 NCREPT Microgrid System Overview

The NCREPT is a $5million test facility, which is at the Arkansas Research and Technology Park along with the University of Arkansas Engineering Research Center (ENRC). This facility was built in 2005 as a result of the 2003 Northeast Blackout and has ever since used for research into investigating advanced power electronics solutions for the electric power grid and

Fig. 4. NCREPT test facility building at the Arkansas engineering research center [26].

transportation applications. In Fig. 4 shown below, a photograph of the NCREPT building, the service entrance transformer and the facility transformers are shown.

The facility transformers are utilized for the microgrid testbed configuration. Fig. 5 shows a one-line diagram schematic representing the microgrid testbed, and in Fig. 6 the bay area inside the facility is shown. NCREPT serves as a cost-effective test facility for universities, businesses and national labs with a pay-per-use structure. Research areas include but are not limited to designing and testing of advanced solid-state solutions for control technologies with a focus on grid reliability, power interface applications, transportation (automotive, aerospace,..) and energy exploration. Other centers associated with NCREPT are the grid-connected advanced power electronics systems (GRAPES), the vertically integrated center for transformative energy research (VICTER) and the high density electronic center (HiDEC). A microgrid testbed has been built at NCREPT to promote research in the areas of microgrid, smart-grid systems, and distributed energy integration to the grid [11].

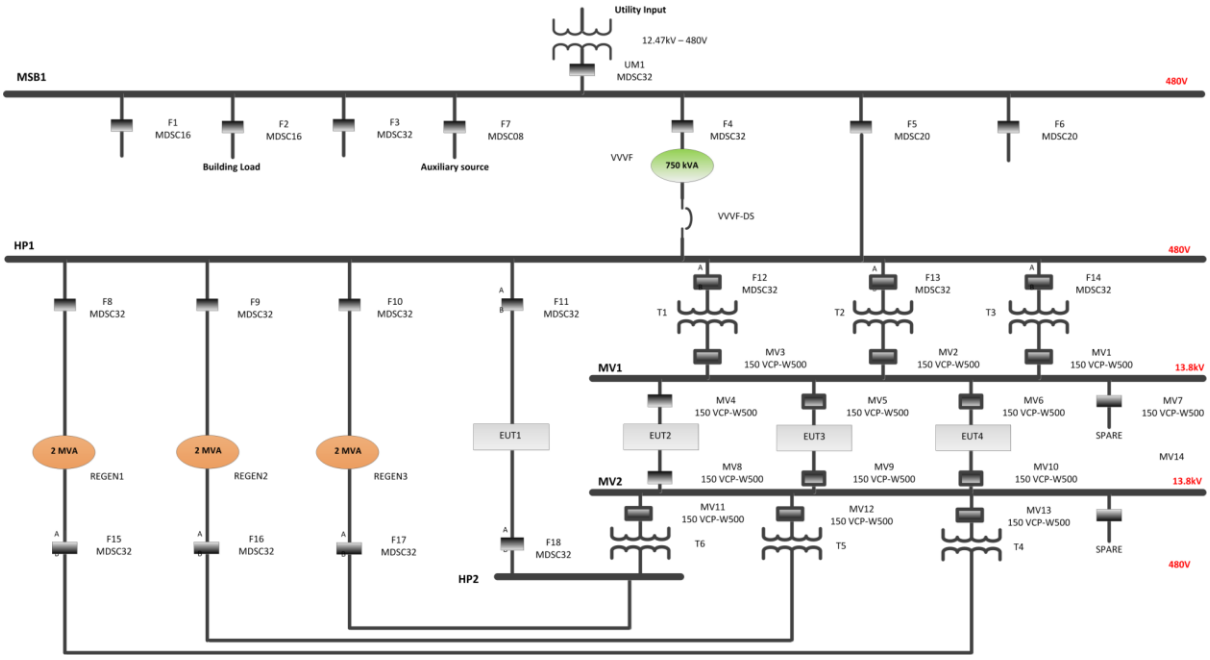


Fig. 5. NCREPT one-line diagram [26].

The NCREPT facility is designed to allow different microgrid configurations and can therefore be used to test many types of devices and designs. For example, Fig. 1 shows an ac microgrid while Fig. 7 demonstrates an ac-dc hybrid one.

As it is detailed in the subsequent chapters, the microgrid system on which the thesis focuses is inspired by that at NCREPT shown in Fig. 1.

Fig. 6. NCREPT bay area [26].

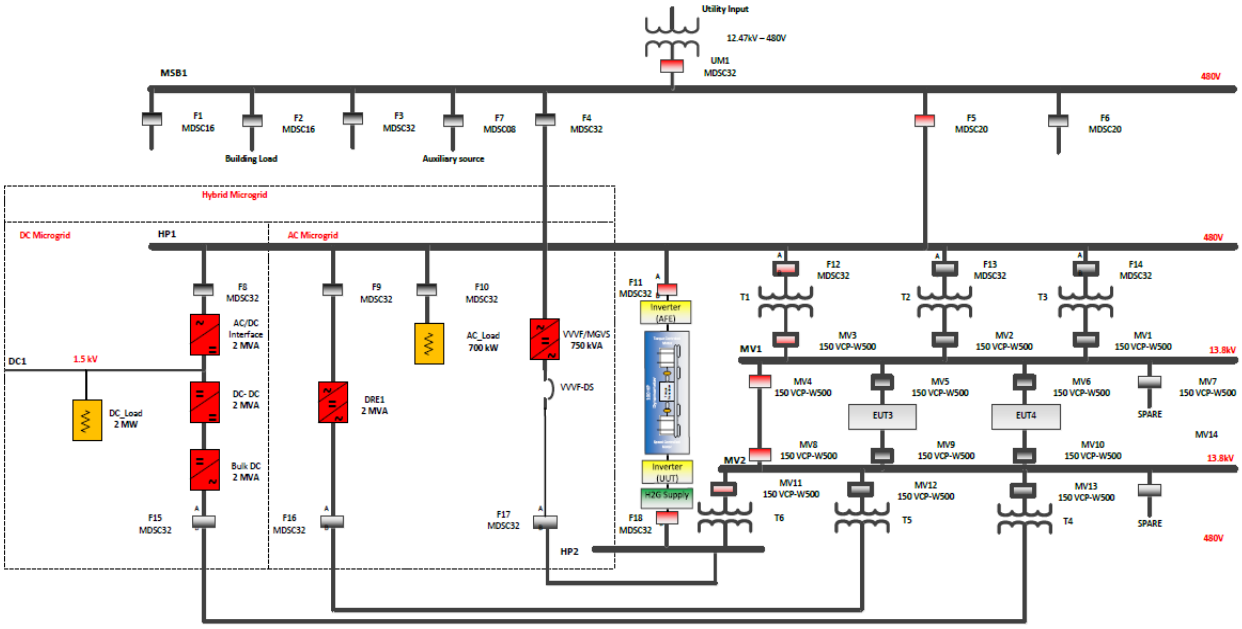


Fig. 7. Hybrid microgrid configuration [26].

The back-to-back converter topology in Fig. 8, which is the backbone of the system, is used for both the regenerative (REGEN) and the variable voltage variable frequency (VVVF) drives. The parameters for the NCREPT microgrid system are summarized in Appendix A.

### II.3 Direct-Quadrature-Zero (dq0) Transformation

The well-known dqo transformation constitutes a mathematical transmutation, which is often used to simplify the analysis of three-phase quantities (voltages, currents, fluxes, etc...). The transformation is accomplished through a mathematical projection of the three-phase phasors onto a rotating reference frame such as it is shown in Fig. 9. The transformation results in two non-zero constants (d and q) and one zero component if the reference frame rotates at the same frequency as that of the three-phase quantities and if the latter are balanced. It is important to note that the dq0 transformation differs from the Park's one in that the former is power invariant and the latter is not. However, for the following mathematical derivations Park's transformation is used for simplicity since they only differ by a constant multiplicand.

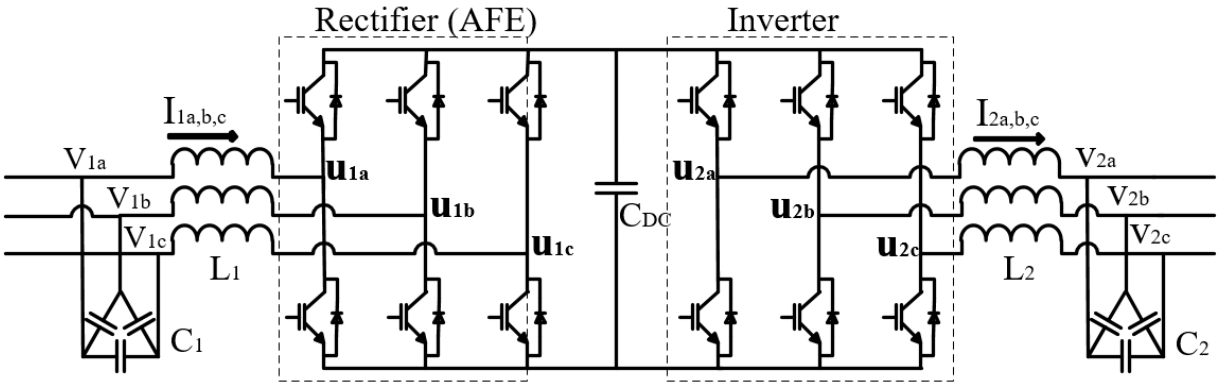


Fig. 8. Back-to-back topology for the Regen and the VVVF drives

### III.3.a Direct Transformation: ABC to dq0

For a balanced voltage triple phase system, the transformation of a, b and c quantities is given by equation (2.1) [24].

$$\begin{bmatrix} x_d \\ x_q \end{bmatrix} = \frac{2}{3}\begin{bmatrix} cos(\theta) & cos(\theta - \frac{2\pi}{3}) & cos(\theta + \frac{2\pi}{3}) \\ -sin(\theta) & -sin(\theta - \frac{2\pi}{3}) & -sin(\theta + \frac{2\pi}{3}) \end{bmatrix}\begin{bmatrix} x_a \\ x_b \\ x_c \end{bmatrix} \tag{2.1}$$

Where $\begin{cases} x_a = X_p \cos\theta_g \\ x_b = X_p \cos\left(\theta_g - \frac{2\pi}{3}\right) \\ x_c = X_p \cos\left(\theta_g + \frac{2\pi}{3}\right) \end{cases}$ and $\theta_g$ is the grid angle.

It follows from (2.1) that:

$$\begin{aligned} x_d &= \frac{2}{3}\left(\cos\theta\, x_a + \cos\left(\theta - \frac{2\pi}{3}\right)x_b + \cos\left(\theta + \frac{2\pi}{3}\right)x_c\right) \\ &= \frac{2}{3}\left(X_p \cos\theta \cos\theta_g + X_p \cos\left(\theta - \frac{2\pi}{3}\right)\cos\left(\theta_g - \frac{2\pi}{3}\right) + X_p \cos\left(\theta + \frac{2\pi}{3}\right)\cos\left(\theta_g + \frac{2\pi}{3}\right)\right) \\ &= \frac{2}{3}\left(\frac{X_p}{2}\left(3\cos(\theta - \theta_g) + \cos(\theta + \theta_g) + \cos\left(\theta + \theta_g - \frac{4\pi}{3}\right) + \cos\left(\theta + \theta_g + \frac{4\pi}{3}\right)\right)\right) \end{aligned}$$

$$x_d = \frac{2}{3}\left(\frac{3X_p}{2}\cos(\theta - \theta_g)\right) = X_p \cos(\theta - \theta_g) \tag{2.2}$$

$$\begin{aligned} x_q &= \frac{2}{3}\left(-\sin\theta\, x_a - \sin\left(\theta - \frac{2\pi}{3}\right)x_b - \sin\left(\theta + \frac{2\pi}{3}\right)x_c\right) \\ &= \frac{2}{3}\left(-X_p \sin\theta \cos\theta_g - X_p \sin\left(\theta - \frac{2\pi}{3}\right)\cos\left(\theta_g - \frac{2\pi}{3}\right) - X_p \sin\left(\theta + \frac{2\pi}{3}\right)\cos\left(\theta_g + \frac{2\pi}{3}\right)\right) \end{aligned}$$

$$x_q = \frac{2}{3}\left(-\frac{3X_p}{2}sin(\theta - \theta_g)\right) = -X_p\, sin(\theta - \theta_g) \tag{2.3}$$

The phase difference is constant if both $\theta$ and $\theta_g$ have the same frequency, and it is given by equation (2.4). Where $\theta$ is the rotation angle for the rotating reference frame, and $\theta_g$ is the electrical angle of the three-phase quantities. In this case, both the direct axis component $x_d$ and the quadrature axis component $x_q$ are constants.

$$\phi = \theta - \theta_g \tag{2.4}$$

### III.3.b Indirect Transformation: ABC to αβ0 and αβ0 to dq0

By using an intermediate transformation, the same results can be obtained as follows:

⇨ First, the transformation from ABC to αβ is accomplished using equation (2.5) as follows:

$$\begin{bmatrix} x_\alpha \\ x_\beta \end{bmatrix} = \frac{2}{3}\begin{bmatrix} 1 & -\frac{1}{2} & -\frac{1}{2} \\ 0 & \frac{\sqrt{3}}{2} & -\frac{\sqrt{3}}{2} \end{bmatrix}\begin{bmatrix} x_a \\ x_b \\ x_c \end{bmatrix} \tag{2.5}$$

$$\begin{aligned} x_\alpha &= \frac{2}{3}\left(x_a - \frac{1}{2}x_b - \frac{1}{2}x_c\right) \\ &= \frac{2}{3}\left(X_p cos\,\theta_g - \frac{1}{2}X_p cos\left(\theta_g - \frac{2\pi}{3}\right) - \frac{1}{2}X_p cos\left(\theta_g + \frac{2\pi}{3}\right)\right) = \frac{2}{3}\left(\frac{3}{2}X_p cos\,\theta_g\right) \\ &= X_p\, cos\,\theta_g \end{aligned}$$

$$x_\alpha = X_p cos\,\theta_g \tag{2.6}$$

$$\begin{aligned} x_\beta &= \frac{2}{3}\left(0\, x_a + \frac{\sqrt{3}}{2}x_b - \frac{\sqrt{3}}{2}x_c\right) \\ &= \frac{2}{3}\left(0 + \frac{\sqrt{3}}{2}X_p\, cos\left(\theta_g - \frac{2\pi}{3}\right) - \frac{\sqrt{3}}{2}X_p\, cos\left(\theta_g + \frac{2\pi}{3}\right)\right) = \frac{2}{3}\left(\frac{3}{2}X_p sin\,\theta_g\right) = X_p sin\,\theta_g \end{aligned}$$

$$x_\beta = X_p \sin\theta_g \tag{2.7}$$

⇨ In the same manner, the transformation from αβ to dq is accomplished using equation (2.8) as follows:

$$\begin{bmatrix} x_d \\ x_q \end{bmatrix} = \begin{bmatrix} cos(\theta) & sin(\theta) & 0 \\ -sin(\theta) & cos(\theta) & 0 \end{bmatrix} \begin{bmatrix} x_\alpha \\ x_\beta \end{bmatrix} \tag{2.8}$$

$$x_d = cos(\theta)\ x_\alpha + sin(\theta)\, x_\beta = X_p\, cos(\theta)\ cos\,\theta_g + X_p\, sin(\theta)\, sin\,\theta_g$$

$$= X_p \left( \frac{1}{2} \left( cos(\theta - \theta_g) + cos(\theta + \theta_g) \right) + \frac{1}{2} \left( cos(\theta - \theta_g) - cos(\theta + \theta_g) \right) \right)$$

$$x_d = X_p\, cos(\theta - \theta_g) \tag{2.9}$$

$$x_q = -sin(\theta)\, x_\alpha + cos(\theta)\, x_\beta = -X_p\, sin(\theta)\, cos\,\theta_g + X_p\, cos(\theta)\, sin\,\theta_g$$

$$= X_p \left( -\frac{1}{2} \left( sin(\theta + \theta_g) - sin(\theta - \theta_g) \right) + \frac{1}{2} \left( sin(\theta + \theta_g) + sin(\theta - \theta_g) \right) \right)$$

$$x_q = -X_p\, sin(\theta - \theta_g) \tag{2.10}$$

From the above derivations, it can be concluded that both the direct and indirect transformations yield the same results since (2.2) is the same as (2.9) and (2.3) equals (2.10).

### III.3.c Graphical Representation

Fig. 9 shows the grahical representaion for different methods used to transform three phase sinusoidally varying quantities in two constant quanties. The different sets of equations derived in the previous section are extensively used in chapter III to accomplish the transformation from three phase coordinates to the rotating coordinates. The system model is modelled in terms of the change in inductor current or capacitor voltage, and the theory covered by this chapter is used to simplify the obtained model.

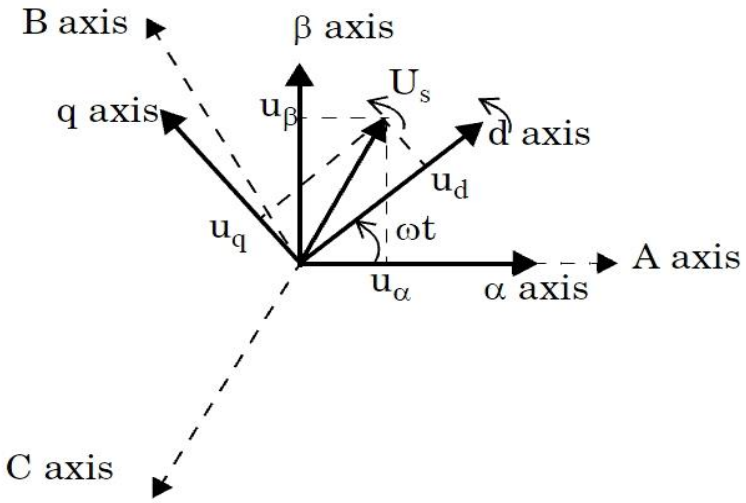


Fig. 9. Geometric relationship between ABC, αβ0, and dqo reference frames [12].

# CHAPTER III MICROGRID SYSTEM MODELING

## III.1 Introduction

This chapter covers the mathematical model derivations for the microgrid system introduced in the previous chapters and covered in [27], and [28]. The obtained model is nonlinear in nature because of the switching of power electronic devices, and must be linearized in order to apply the proposed controller. To that end, the technique and process involved in linearizing it are covered in this chapter as well. Finally, this chapter covers the model validation process used to make sure that the linearized mathematical model and the actual modelled system have the same dynamics and converge to the same steady state values with minimal error.

There is a continuous need for improved modeling and vigorous simulation to analyze different scenarios in order to characterize the impact of a rapidly increasing deployment of renewable resources, as well as that of energy storage, on the modern electrical grid [15]. That being said, accuracy in mathematical models and realistic simulations are essential to drawing reasonable and effective conclusions. As a result, this chapter is devoted on the techniques used to model the microgrid system of Fig. 10 and validating the obtained mathematical model.

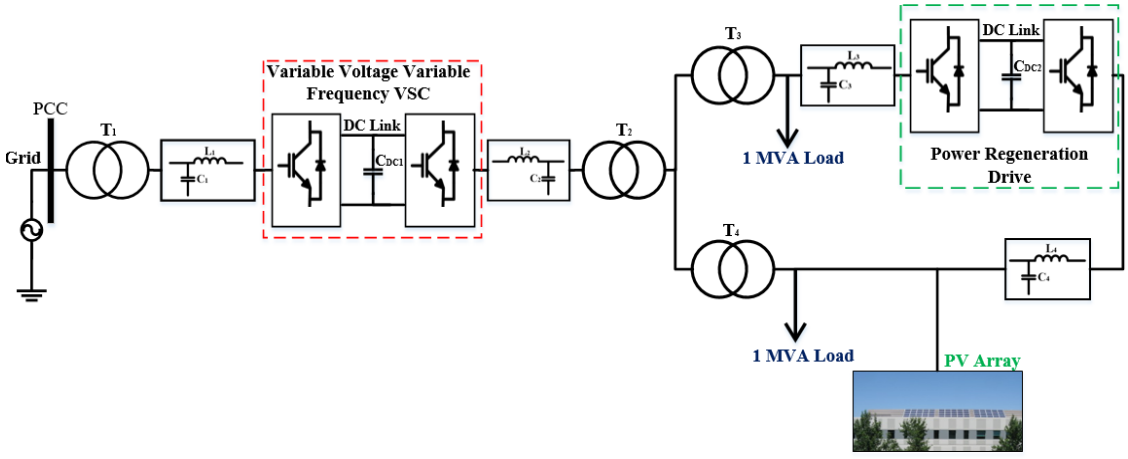


Fig. 10. Cascaded converters-based microgrid system [27].

### III.2 Circuit Model

This project focuses on the analysis of the microgrid system presented in Fig. 10, which was inspired by the NCREPT microgrid testbed discussed in the previous chapters. A few modifications have been made to the microgrid in Fig. 1, and the resulting one is shown in Fig. 10. These changes include a photovoltaic (PV) array system added as a backup power source and two loads.

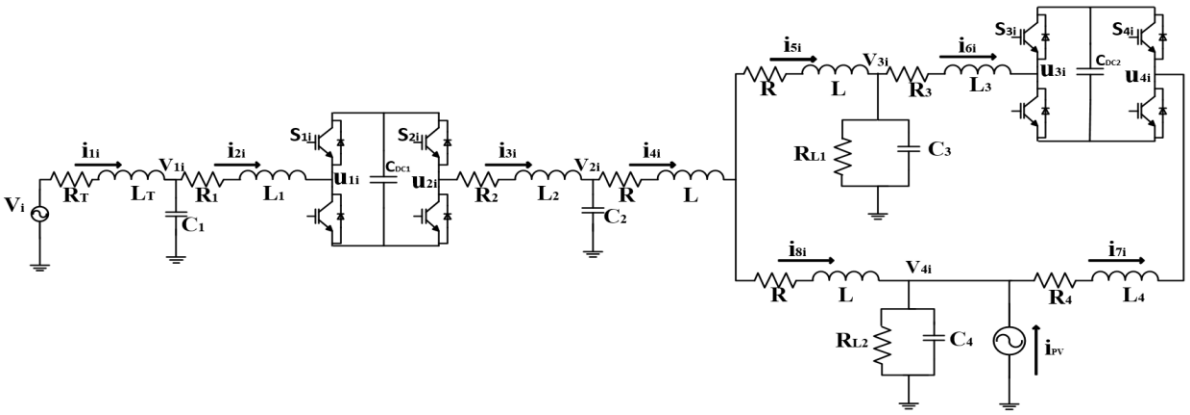


Fig. 11. Single phase equivalent circuit for network controller development [27].

TABLE I
SYSTEM COMPONENT AND PARAMETER VALUES

| Component | Symbol | Nominal Value | | | Component | Symbol | Nominal Value | |
|---|---|---|---|---|---|---|---|---|
| Service XFR | $R_T$ | 0.23 | mΩ | | 3 MV XFR | R | 0.23 | mΩ |
| | $L_T$ | 6.1 | µH | | | L | 6.1 | µH |
| LC Filter 1 | $R_1$ | 207 | mΩ | | LC Filter 4 | $R_4$ | 3.8 | mΩ |
| | $L_1$ | 110 | µH | | | $L_4$ | 20 | µH |
| | $C_1$ | 2880 | µF | | | $C_4$ | 1440 | µF |
| LC Filter 2 | $R_2$ | 207 | mΩ | | Load 1 | $R_{L1}$ | 0.23 | Ω |
| | $L_2$ | 110 | µH | | Load 2 | $R_{L2}$ | 0.23 | Ω |
| | $C_2$ | 2880 | µF | | VVVF dc-link cap. | $C_{DC1}$ | 25200 | µF |
| LC Filter 3 | $R_3$ | 3.2 | mΩ | | Regen dc-link cap. | $C_{DC2}$ | 37800 | µF |
| | $L_3$ | 20 | µH | | System frequency | Ω | 120π | rad/s |
| | $C_3$ | 1440 | µF | | System voltage | $V_{RMS}$ | 480 | V |

Fig. 11 shows a per phase equivalent circuit of the microgrid system from which a mathematical model is derived using the Kirchhoff's current and voltage laws. The PV array and its output inverter are modelled as a three-phase current source for simplicity. This analysis assumes the PV array system constitutes an independent stable source capable of supplying a given power to the rest of the system. Also, each load and the adjacent shunt capacitor forming an LC-filter are modelled in Fig. 11 as a parallel shunt RC circuit.

Table I summarizes the equivalent overall component values for the circuit demonstrated in Fig. 11, and appendix A provides the details for these components and their arrangement on the physical system at NCREPT. The component values shown in Table I are the same values used for simulations and designs, which are covered in chapters IV through VI.

### III.3 Nonlinear Mathematical Model

To develop the nonlinear mathematical model in terms of differential equations (DEs), the circuit shown in Fig. 11 is solved using basic Kirchhoff's current and voltage laws. This section is centered on the derivation of the mathematical equations, which constitutes the system model. Throughout this section, the symbol $\mu$ is used to represent the switching function for power electronics devices, and the subscript $i$ is used to denote the $A$, $B$ and $C$ three phase quantities. Moreover, the transformation of the obtained model into the dq0 synchronous frame also presented at the end of this section.

The per-phase circuit, which represents the microgrid is shown in Fig. 11. A closer look at the obtained this circuit indicates that there are 8 different inductor currents and 6 different capacitor voltages. These quantities determine how many state variables the dynamic model must have. Since it has been shown that each triple of three-phase quantities results in 2 variables in the *dq0* rotating reference, one can forecast 26 state variables: 18 inductor currents, 8 capacitor

voltages and the 2 dc-link voltages. However, this is not the case. In fact, at least 2 of these states variables can be eliminated as follows. Fig. 11 shows that the inductor currents $i_{4i}$ can be given by the sum of inductor currents $i_{5i}$ and $i_{8i}$ as expressed in equation (3.3). Because of this relationship between the three currents, any fixed values for 2 of these 3 inductor currents give a constant value for the remaining one. Therefore, if 2 of these currents are regulated buy a controller action then the third one is also controlled indirectly. As a result, these inductor currents are said to be linearly dependent, and one of them must be mathematically eliminated. Equations (3.1) to (3.7) summarize the elimination process taken to obtain coupled differential equations for currents $i_{4i}$ and $i_{5i}$.

Considering the circuit in Fig. 11, nodal analysis is first performed for the loop containing $v_{2i}$, $i_{4i}$, $i_{8i}$ and $v_{4i}$. The resulting differential equation is given in (3.1), which indicates that the sum of voltage drops in a closed loop is zero. Using the same analysis for the loop containing $v_{2i}$, $i_{4i}$, $i_{8i}$ and $v_{4i}$, equation (3.2) is obtained for the second current. In addition, the equation, which relates the 3 currents is given in (3.3).

$$v_{2i} - Ri_{4i} - L\frac{di_{4i}}{dt} - Ri_{8i} - L\frac{di_{8i}}{dt} - v_{4i} = 0. \tag{3.1}$$

$$v_{2i} - Ri_{4i} - L\frac{di_{4i}}{dt} - Ri_{5i} - L\frac{di_{5i}}{dt} - v_{3i} = 0. \tag{3.2}$$

$$i_{8i} = i_{4i} - i_{5i}. \tag{3.2}$$

From the above 3 equations, one derives 2 DEs having a single derivative term as follows. First, equation (3.3) is used to substitute for $i_{8i}$ in (3.1). The resulting expression is given in (3.4). Secondly, equation (3.2) is rearranged to give the DE in (3.5). At this point, $i_{8i}$ has been substituted

in both equations (3.4) and (3.5). Finally, the sum of equations (3.4) and (3.5) gives the final DE (3.6) for the current $i_{4i}$. Similarly, the final DE for current $i_{5i}$ is obtained by multiplying equation (3.5) by 2 and subtracting (3.4) from the resulting expression.

$$2L\frac{di_{4i}}{dt} - L\frac{di_{5i}}{dt} = -2Ri_{4i} + Ri_{5i} + v_{2i} - v_{4i} \tag{3.4}$$

$$L\frac{di_{4i}}{dt} + L\frac{di_{5i}}{dt} = -Ri_{4i} - Ri_{5i} + v_{2i} - v_{3i} \tag{3.5}$$

$$3L\frac{di_{4i}}{dt} = -3Ri_{4i} + 2v_{2i} - v_{3i} - v_{4i} \tag{3.6}$$

$$3L\frac{di_{5i}}{dt} = -3Ri_{5i} + v_{2i} - 2v_{3i} + v_{4i} \tag{3.7}$$

Equations (3.3), (3.6), and (3.7) are sufficient to represent the dynamics for inductor currents $i_{4i}$, $i_{5i}$ and $i_{8i}$. The DE for rest of inductor currents, as shown in Fig. 11, are obtained using nodal analysis for the closed loop containing each specific current. Equations (3.8) through (3.12) give the derived mathematical equations.

$$v_i - L_T\frac{di_{1i}}{dt} - R_T i_{1i} - v_{1i} = 0. \tag{3.8}$$

$$v_{1i} - L_1\frac{di_{2i}}{dt} - R_1 i_{2i} - u_{1i} = 0. \tag{3.9}$$

$$u_{2i} - L_2\frac{di_{3i}}{dt} - R_2 i_{3i} - v_{2i} = 0. \tag{3.10}$$

$$v_{3i} - L_3 \frac{di_{6i}}{dt} - R_3 i_{6i} - u_{3i} = 0 \tag{3.11}$$

$$v_{4i} - L_4 \frac{di_{7i}}{dt} - R_4 i_{7i} - u_{4i} = 0 \tag{3.12}$$

To determine the DEs, which express the capacitor voltages, a different approach is taken instead of using nodal analysis. In addition, it is well known that the change in a capacitor voltage is proportional to the current passing through it. Therefore, these two laws are used to derive equations (3.13) through (3.18), which express the change in voltage for each capacitor in the circuit model.

$$\frac{dv_{1i}}{dt} = \frac{1}{C_1}(i_{1i} - i_{2i}) \tag{3.13}$$

$$\frac{dv_{dc1}}{dt} = \frac{1}{C_{dc1}} \left( \sum_{i=a,b,c} \mu_{1i} i_{2i} - \sum_{i=a,b,c} \mu_{2i} i_{3i} \right) \tag{3.14}$$

$$\frac{dv_{2i}}{dt} = \frac{1}{C_2} (i_{3i} - i_{4i}) \tag{3.15}$$

$$\frac{dv_{3i}}{dt} = \frac{1}{C_3} \left( i_{5i} - i_{6i} - \frac{v_{3i}}{R_{L1}} \right) \tag{3.16}$$

$$\frac{dv_{4i}}{dt} = \frac{1}{C_4} \left( i_{4i} - i_{5i} - i_{7i} - \frac{v_{4i}}{R_{L2}} + i_{PV} \right) \tag{3.17}$$

$$\frac{dv_{dc2}}{dt} = \frac{1}{C_{dc2}} \left( \sum_{i=a,b,c} \mu_{3i} i_{6i} + \sum_{i=a,b,c} \mu_{4i} i_{7i} \right) \tag{3.18}$$

The obtained DEs, (3.6) through (3.18) and the relation given in (3.3), form the mathematical model for the microgrid shown in Fig. 10 and Fig. 11. This model is summarized by the system of DEs (3.19)

$$
\begin{cases}
L_T \dfrac{di_{1i}}{dt} = -R_T i_{1i} - v_{1i} + v_i \\
L_1 \dfrac{di_{2i}}{dt} = -R_1 i_{2i} - u_{1i} + v_{1i} \\
L_2 \dfrac{di_{3i}}{dt} = -R_2 i_{3i} + u_{2i} - v_{2i} \\
3L \dfrac{di_{4i}}{dt} = -3R i_{4i} + 2v_{2i} - v_{3i} - v_{4i} \\
3L \dfrac{di_{5i}}{dt} = -3R i_{5i} + v_{2i} - 2v_{3i} + v_{4i} \\
L_3 \dfrac{di_{6i}}{dt} = -R_3 i_{6i} - u_{3i} + v_{3i} \\
L_4 \dfrac{di_{7i}}{dt} = -R_4 i_{7i} - u_{4i} + v_{4i} \\
C_{dc1} \dfrac{dv_{DC1}}{dt} = \sum_{i=a,b,c} \mu_{1i} i_{2i} - \sum_{i=a,b,c} \mu_{2i} i_{3i} \\
C_{dc2} \dfrac{dv_{DC2}}{dt} = \sum_{i=a,b,c} \mu_{3i} i_{6i} + \sum_{i=a,b,c} \mu_{4i} i_{7i} \\
C_1 \dfrac{dv_{1i}}{dt} = i_{1i} - i_{2i} \\
C_2 \dfrac{dv_{2i}}{dt} = i_{3i} - i_{4i} \\
C_3 \dfrac{dv_{3i}}{dt} = i_{5i} - i_{6i} - \dfrac{v_{3i}}{R_{L1}} \\
C_4 \dfrac{dv_{4i}}{dt} = i_{4i} - i_{5i} - i_{7i} - \dfrac{v_{4i}}{R_{L2}} + i_{PV} \\
i_{8i} = i_{4i} - i_{5i}
\end{cases}
\tag{3.19}
$$

The transformation from the three-phase coordinates of the resulting time-varying sinusoidal variable of (3.19) to the two-coordinate synchronous rotating frame leads to the mathematical model described by the system of equations in (3.20) [25]. It follows that the system

of equations given in (3.20) constitutes the nonlinear dynamic model of the microgrid system in Fig. 10.

$$
\begin{cases}
\frac{d}{dt}\begin{bmatrix} i_{1d} \\ i_{1q} \end{bmatrix} = \frac{1}{L_T}\begin{bmatrix} -R_T & \omega L_T \\ -\omega L_T & -R_T \end{bmatrix}\begin{bmatrix} i_{1d} \\ i_{1q} \end{bmatrix} - \frac{1}{L_T}\begin{bmatrix} v_{1d} \\ v_{1q} \end{bmatrix} + \frac{1}{L_T}\begin{bmatrix} v_d \\ v_q \end{bmatrix} \\
\frac{d}{dt}\begin{bmatrix} i_{2d} \\ i_{2q} \end{bmatrix} = \frac{1}{L_1}\begin{bmatrix} -R_1 & \omega L_1 \\ -\omega L_1 & -R_1 \end{bmatrix}\begin{bmatrix} i_{2d} \\ i_{2q} \end{bmatrix} - \frac{v_{Cdc1}}{L_1}\begin{bmatrix} \mu_{1d} \\ \mu_{1q} \end{bmatrix} + \frac{1}{L_1}\begin{bmatrix} v_{1d} \\ v_{1q} \end{bmatrix} \\
\frac{d}{dt}\begin{bmatrix} i_{3d} \\ i_{3q} \end{bmatrix} = \frac{1}{L_2}\begin{bmatrix} -R_2 & \omega L_2 \\ -\omega L_2 & -R_2 \end{bmatrix}\begin{bmatrix} i_{3d} \\ i_{3q} \end{bmatrix} + \frac{v_{Cdc1}}{L_2}\begin{bmatrix} \mu_{2d} \\ \mu_{2q} \end{bmatrix} - \frac{1}{L_2}\begin{bmatrix} v_{2d} \\ v_{2q} \end{bmatrix} \\
\frac{d}{dt}\begin{bmatrix} i_{4d} \\ i_{4q} \end{bmatrix} = \frac{1}{L}\begin{bmatrix} -R & \omega L \\ -\omega L & -R \end{bmatrix}\begin{bmatrix} i_{4d} \\ i_{4q} \end{bmatrix} + \frac{2}{3L}\begin{bmatrix} v_{2d} \\ v_{2q} \end{bmatrix} - \frac{1}{3L}\begin{bmatrix} v_{3d} \\ v_{3q} \end{bmatrix} - \frac{1}{3L}\begin{bmatrix} v_{4d} \\ v_{4q} \end{bmatrix} \\
\frac{d}{dt}\begin{bmatrix} i_{5d} \\ i_{5q} \end{bmatrix} = \frac{1}{L}\begin{bmatrix} -R & \omega L \\ -\omega L & -R \end{bmatrix}\begin{bmatrix} i_{5d} \\ i_{5q} \end{bmatrix} + \frac{1}{3L}\begin{bmatrix} v_{2d} \\ v_{2q} \end{bmatrix} - \frac{2}{3L}\begin{bmatrix} v_{3d} \\ v_{3q} \end{bmatrix} + \frac{1}{3L}\begin{bmatrix} v_{4d} \\ v_{4q} \end{bmatrix} \\
\frac{d}{dt}\begin{bmatrix} i_{6d} \\ i_{6q} \end{bmatrix} = \frac{1}{L_3}\begin{bmatrix} -R_3 & \omega L_3 \\ -\omega L_3 & -R_3 \end{bmatrix}\begin{bmatrix} i_{6d} \\ i_{6q} \end{bmatrix} - \frac{v_{Cdc2}}{L_3}\begin{bmatrix} \mu_{3d} \\ \mu_{3q} \end{bmatrix} + \frac{1}{L_3}\begin{bmatrix} v_{3d} \\ v_{3q} \end{bmatrix} \\
\frac{d}{dt}\begin{bmatrix} i_{7d} \\ i_{7q} \end{bmatrix} = \frac{1}{L_4}\begin{bmatrix} -R_4 & \omega L_4 \\ -\omega L_4 & -R_4 \end{bmatrix}\begin{bmatrix} i_{7d} \\ i_{7q} \end{bmatrix} - \frac{v_{Cdc2}}{L_4}\begin{bmatrix} \mu_{4d} \\ \mu_{4q} \end{bmatrix} + \frac{1}{L_4}\begin{bmatrix} v_{4d} \\ v_{4q} \end{bmatrix} \\
\frac{d\, v_{CDC1}}{dt} = \frac{1}{C_{DC}}\Big(\big(\mu_{1d} i_{2d} + \mu_{1q} i_{2q}\big) - \big(\mu_{2d} i_{3d} + \mu_{2q} i_{3q}\big)\Big) \\
\frac{d\, v_{CDC2}}{dt} = \frac{1}{C_{DC}}\Big(\big(\mu_{3d} i_{6d} + \mu_{3q} i_{6q}\big) + \big(\mu_{4d} i_{7d} + \mu_{4q} i_{7q}\big)\Big) \\
\frac{d}{dt}\begin{bmatrix} v_{1d} \\ v_{1q} \end{bmatrix} = \frac{1}{C_1}\begin{bmatrix} i_{1d} \\ i_{1q} \end{bmatrix} - \frac{1}{C_1}\begin{bmatrix} i_{2d} \\ i_{2q} \end{bmatrix} + \begin{bmatrix} 0 & \omega \\ -\omega & 0 \end{bmatrix}\begin{bmatrix} v_{1d} \\ v_{1q} \end{bmatrix} \\
\frac{d}{dt}\begin{bmatrix} v_{2d} \\ v_{2q} \end{bmatrix} = \frac{1}{C_2}\begin{bmatrix} i_{3d} \\ i_{3q} \end{bmatrix} - \frac{1}{C_2}\begin{bmatrix} i_{4d} \\ i_{4q} \end{bmatrix} + \begin{bmatrix} 0 & \omega \\ -\omega & 0 \end{bmatrix}\begin{bmatrix} v_{2d} \\ v_{2q} \end{bmatrix} \\
\frac{d}{dt}\begin{bmatrix} v_{3d} \\ v_{3q} \end{bmatrix} = \frac{1}{C_3}\begin{bmatrix} i_{5d} \\ i_{5q} \end{bmatrix} - \frac{1}{C_3}\begin{bmatrix} i_{6d} \\ i_{6q} \end{bmatrix} + \frac{1}{R_{L1}C_3}\begin{bmatrix} -1 & \omega R_{L1}C_3 \\ -\omega R_{L1}C_3 & -1 \end{bmatrix}\begin{bmatrix} v_{3d} \\ v_{3q} \end{bmatrix} \\
\frac{d}{dt}\begin{bmatrix} v_{4d} \\ v_{4q} \end{bmatrix} = \frac{1}{C_4}\left(\begin{bmatrix} i_{4d} \\ i_{4q} \end{bmatrix} - \begin{bmatrix} i_{5d} \\ i_{5q} \end{bmatrix} - \begin{bmatrix} i_{7d} \\ i_{7q} \end{bmatrix}\right) + \frac{1}{R_{L2}C_4}\begin{bmatrix} -1 & \omega R_{L2}C_4 \\ -\omega R_{L2}C_4 & -1 \end{bmatrix}\begin{bmatrix} v_{4d} \\ v_{4q} \end{bmatrix} + \frac{1}{C_4}\begin{bmatrix} i_{PVd} \\ i_{PVq} \end{bmatrix} \\
\begin{bmatrix} i_{8d} \\ i_{8q} \end{bmatrix} = \begin{bmatrix} i_{4d} \\ i_{4q} \end{bmatrix} - \begin{bmatrix} i_{5d} \\ i_{5q} \end{bmatrix}
\end{cases}
\tag{3.20}
$$

## III.4 Model Linearization for Controller Development

The model obtained in the two-coordinate synchronous rating frame simplifies the controller development because the inductor currents and capacitor voltages are dc quantities as opposed to those in the three-phase coordinate system. However, the model still poses a level of

complexity in that the system of equations in (3.20) is not linear because there are terms of products of time-varying switching functions and state variables. This challenge is overcome by linearizing the model in (3.20) using the first-order terms on Taylor series expansion around the system's equilibrium point.

To derive the linearized model, (3.20) is written in the state space form, which is expressed by equations in (3.21), where *x* represents the state variable matrix, *u* denotes the controlled-input, $u_d$ is the disturbance input matrix and *y* is the output vectors. The matrices *A*, *B*, *F* and *C* are the non-constant respective matrices of appropriate sizes with the notation of [23] adopted.

$$\begin{cases} \dot{x} = Ax + Bu + Fu_d \\ y = Cx \end{cases} \qquad with\ x \in \mathbb{R}^n, u \in \mathbb{R}^p, u_d \in \mathbb{R}^m\ and\ y \in \mathbb{R}^q. \tag{3.21}$$

Suppose two functions f and g defined in (3.22) and (3.23) as follows:

$$\dot{x} = f(x,u,u_d) = [f_1(x,u,u_d)\ f_2(x,u,u_d) \dots\ f_n(x,u,u_d)]^T, \tag{3.22}$$

$$\text{and} \quad y = g(x,u,u_d) = [g_1(x,u,u_d)\ g_2(x,u,u_d) \dots\ g_q(x,u,u_d)]^T. \tag{3.23}$$

These two functions can be approximated by the first order term of Taylor series expansion as follow:

$$f(x,u,u_d) \approx f(\bar{x},\bar{u},\bar{u}_d) + \frac{\partial f}{\partial x}\Big|_{(\bar{x},\bar{u},\bar{u}_d)} \Delta x + \frac{\partial f}{\partial u}\Big|_{(\bar{x},\bar{u},\bar{u}_d)} \Delta u + \frac{\partial f}{\partial u_d}\Big|_{(\bar{x},\bar{u},\bar{u}_d)} \Delta u_d\ , \tag{3.24}$$

$$g(x,u,u_d) \approx g(\bar{x},\bar{u},\bar{u}_d) + \frac{\partial g}{\partial x}\Big|_{(\bar{x},\bar{u},\bar{u}_d)} \Delta x + \frac{\partial g}{\partial u}\Big|_{(\bar{x},\bar{u},\bar{u}_d)} \Delta u + \frac{\partial g}{\partial u_d}\Big|_{(\bar{x},\bar{u},\bar{u}_d)} \Delta u_d. \tag{3.25}$$

Where $(\bar{x},\bar{u},\bar{u}_d)$ represents the equilibrium point and the quantities $\Delta x = x - \bar{x}$, $\Delta u = u - \bar{u}$ and $\Delta u = u_d - \bar{u}_d$ measure the perturbation from that point.

It follows that the linearized system becomes

$$\Delta\dot{x} = \bar{A}\Delta x + \bar{B}\Delta u + \bar{F}\Delta u_d, \tag{3.26}$$

$$\Delta y = \bar{C}\Delta x + \bar{D}\Delta u + \bar{M}\Delta u_d, \tag{3.27}$$

where $\bar{D}$ and $\bar{M}$ are zero matrices and the rest of the others are given by the expressions below.

$$\bar{A} = \begin{bmatrix} \left.\frac{\partial f_1}{\partial x_1}\right|_{(\bar{x},\bar{u},\bar{u}_d)} & \cdots & \left.\frac{\partial f_1}{\partial x_n}\right|_{(\bar{x},\bar{u},\bar{u}_d)} \\ \vdots & \ddots & \vdots \\ c\left.\frac{\partial f_n}{\partial x_1}\right|_{(\bar{x},\bar{u},\bar{u}_d)} & \cdots & \left.\frac{\partial f_n}{\partial x_n}\right|_{(\bar{x},\bar{u},\bar{u}_d)} \end{bmatrix}, \bar{B} = \begin{bmatrix} \left.\frac{\partial f_1}{\partial u_1}\right|_{(\bar{x},\bar{u},\bar{u}_d)} & \cdots & \left.\frac{\partial f_1}{\partial u_m}\right|_{(\bar{x},\bar{u},\bar{u}_d)} \\ \vdots & \ddots & \vdots \\ \left.\frac{\partial f_n}{\partial u_1}\right|_{(\bar{x},\bar{u},\bar{u}_d)} & \cdots & \left.\frac{\partial f_n}{\partial u_m}\right|_{(\bar{x},\bar{u},\bar{u}_d)} \end{bmatrix},$$

$$\bar{F} = \begin{bmatrix} \left.\frac{\partial f_1}{\partial u_{d1}}\right|_{(\bar{x},\bar{u},\bar{u}_d)} & \cdots & \left.\frac{\partial f_1}{\partial u_{dl}}\right|_{(\bar{x},\bar{u},\bar{u}_d)} \\ \vdots & \ddots & \vdots \\ \left.\frac{\partial f_n}{\partial u_{d1}}\right|_{(\bar{x},\bar{u},\bar{u}_d)} & \cdots & \left.\frac{\partial f_n}{\partial u_{dl}}\right|_{(\bar{x},\bar{u},\bar{u}_d)} \end{bmatrix}, and\ \bar{C} = \begin{bmatrix} \left.\frac{\partial g_1}{\partial x_1}\right|_{(\bar{x},\bar{u},\bar{u}_d)} & \cdots & \left.\frac{\partial g_1}{\partial x_n}\right|_{(\bar{x},\bar{u},\bar{u}_d)} \\ \vdots & \ddots & \vdots \\ c\left.\frac{\partial g_l}{\partial x_1}\right|_{(\bar{x},\bar{u},\bar{u}_d)} & \cdots & \left.\frac{\partial g_l}{\partial x_n}\right|_{(\bar{x},\bar{u},\bar{u}_d)} \end{bmatrix}.$$

Also, $x = [i_{1d} \quad i_{1q} \quad . \quad . \quad . \quad i_{7d} \quad i_{7q} \quad v_{CDC1} \quad v_{CDC2} \quad v_{1d} \quad v_{1q} \quad . \quad . \quad . \quad v_{4d} \quad v_{4q}]^T$,

$u = [\mu_{1d} \quad \mu_{1q} \quad \mu_{2d} \quad \mu_{2q} \quad \mu_{3d} \quad \mu_{3q} \quad \mu_{4d} \quad \mu_{4q}]^T$, $and\ u_d = [v_d \quad v_d \quad i_{PVd} \quad i_{PVq}]^T$.

The system's matrices for the linearized model are given below in a compact form. Explicit forms are provided in appendix E, and their nonzero elements are given in Table II and Table III.

$$\bar{A} = \begin{bmatrix} a_{1,1} & \cdots & a_{1,24} \\ \vdots & \ddots & \vdots \\ a_{24,1} & \cdots & a_{24,24} \end{bmatrix}.$$

$$\bar{B} = \begin{bmatrix} b_{1,1} & \cdots & b_{1,8} \\ \vdots & \ddots & \vdots \\ b_{24,1} & \cdots & b_{24,8} \end{bmatrix}.$$

$$\bar{\mathrm{F}} = \begin{bmatrix} f_{1,1} & \cdots & f_{1,4} \\ \vdots & \ddots & \vdots \\ f_{24,1} & \cdots & f_{24,4} \end{bmatrix}.$$

TABLE II
STATE MATRIX ELEMENTS

| Element | Formula | Element | Formula | Element | Formula |
|---|---|---|---|---|---|
| $a_{1,1}$ | $\frac{R_T}{L_T}$ | $a_{11,12}$ | $\omega$ | $a_{23,7}$ | $\frac{1}{C_4}$ |
| $a_{1,2}$ | $\omega$ | $a_{11,16}$ | $-\frac{\bar{\mu}_{3d}}{L_3}$ | $a_{23,9}$ | $-\frac{1}{C_4}$ |
| $a_{1,17}$ | $-\frac{1}{L_T}$ | $a_{11,21}$ | $\frac{1}{L_3}$ | $a_{23,13}$ | $-\frac{1}{C_4}$ |
| $a_{2,1}$ | $-\omega$ | $a_{12,11}$ | $-\omega$ | $a_{23,23}$ | $-(R_{L2}C_4)^{-1}$ |
| $a_{2,2}$ | $-\frac{R_T}{L_T}$ | $a_{12,12}$ | $-\frac{R_3}{L_3}$ | $a_{23,24}$ | $\omega$ |
| $a_{2,18}$ | $-\frac{1}{L_T}$ | $a_{12,16}$ | $-\frac{\bar{\mu}_{3q}}{L_3}$ | $a_{24,8}$ | $\frac{1}{C_4}$ |
| $a_{3,3}$ | $-\frac{R_1}{L_1}$ | $a_{12,22}$ | $\frac{1}{L_3}$ | $a_{24,10}$ | $-\frac{1}{C_4}$ |
| $a_{3,4}$ | $\omega$ | $a_{13,13}$ | $-\frac{R_4}{L_4}$ | $a_{24,14}$ | $-\frac{1}{C_4}$ |
| $a_{3,15}$ | $-\frac{\bar{\mu}_{1d}}{L_1}$ | $a_{13,14}$ | $\omega$ | $a_{24,23}$ | $-\omega$ |
| $a_{3,17}$ | $\frac{1}{L_1}$ | $a_{13,16}$ | $-\frac{\bar{\mu}_{4d}}{L_4}$ | $a_{24,24}$ | $-\frac{1}{R_{L2}C_4}$ |
| $a_{4,3}$ | $-\omega$ | $a_{13,23}$ | $\frac{1}{L_4}$ | $b_{3,1}$ | $-\frac{\bar{\mathrm{V}}_{DC1}}{L_1}$ |
| $a_{4,4}$ | $-\frac{R_1}{L_1}$ | $a_{14,13}$ | $-\omega$ | $b_{4,2}$ | $-\frac{\bar{\mathrm{V}}_{DC1}}{L_1}$ |
| $a_{4,15}$ | $-\frac{\bar{\mu}_{1q}}{L_1}$ | $a_{14,14}$ | $-\frac{R_4}{L_4}$ | $b_{5,3}$ | $-\frac{\bar{\mathrm{V}}_{DC1}}{L_2}$ |
| $a_{4,18}$ | $\frac{1}{L_1}$ | $a_{14,16}$ | $-\frac{\bar{\mu}_{4q}}{L_4}$ | $b_{6,4}$ | $-\frac{\bar{\mathrm{V}}_{DC1}}{L_2}$ |
| $a_{5,5}$ | $-\frac{R_2}{L_2}$ | $a_{14,24}$ | $\frac{1}{L_4}$ | $b_{11,5}$ | $-\frac{\bar{\mathrm{V}}_{DC2}}{L_3}$ |
| $a_{5,6}$ | $\omega$ | $a_{15,3}$ | $\frac{\bar{\mu}_{1d}}{C_{DC1}}$ | $b_{12,6}$ | $-\frac{\bar{\mathrm{V}}_{DC2}}{L_3}$ |
| $a_{5,15}$ | $\frac{\bar{\mu}_{2d}}{L_4}$ | $a_{15,4}$ | $\frac{\bar{\mu}_{1q}}{C_{DC1}}$ | $b_{13,7}$ | $-\frac{\bar{\mathrm{V}}_{DC2}}{L_4}$ |
| $a_{5,19}$ | $-\frac{1}{L_2}$ | $a_{15,5}$ | $-\frac{\bar{\mu}_{2d}}{C_{DC1}}$ | $b_{14,8}$ | $-\frac{\bar{\mathrm{V}}_{DC2}}{L_3}$ |
| $a_{6,5}$ | $-\omega$ | $a_{15,6}$ | $-\frac{\bar{\mu}_{2q}}{C_{DC1}}$ | $b_{15,1}$ | $\frac{\bar{\mathrm{I}}_{2d}}{V_{DC1}}$ |

TABLE III
STATE MATRIX ELEMENTS (CONT.)

| Element | Formula | Element | Formula | Element | Formula |
|---|---|---|---|---|---|
| $a_{6,6}$ | $-\frac{R_2}{L_2}$ | $a_{16,11}$ | $\frac{\bar{\mu}_{3d}}{C_{DC1}}$ | $b_{15,2}$ | $\frac{\bar{I}_{2q}}{V_{DC1}}$ |
| $a_{6,15}$ | $\frac{\bar{\mu}_{2q}}{L_4}$ | $a_{16,12}$ | $\frac{\bar{\mu}_{3q}}{C_{DC1}}$ | $b_{15,3}$ | $-\frac{\bar{I}_{3d}}{V_{DC1}}$ |
| $a_{6,20}$ | $-\frac{1}{L_2}$ | $a_{16,13}$ | $-\frac{\bar{\mu}_{4d}}{C_{DC1}}$ | $b_{15,4}$ | $-\frac{\bar{I}_{3q}}{V_{DC1}}$ |
| $a_{7,7}$ | $-\frac{R}{L}$ | $a_{16,14}$ | $-\frac{\bar{\mu}_{4q}}{C_{DC1}}$ | $b_{16,5}$ | $\frac{\bar{I}_{6d}}{V_{DC2}}$ |
| $a_{7,8}$ | $\omega$ | $a_{17,1}$ | $\frac{1}{C_1}$ | $b_{16,6}$ | $\frac{\bar{I}_{6q}}{V_{DC2}}$ |
| $a_{7,19}$ | $\frac{2}{3L}$ | $a_{17,3}$ | $-\frac{1}{C_1}$ | $b_{16,7}$ | $\frac{\bar{I}_{7d}}{V_{DC2}}$ |
| $a_{7,21}$ | $-\frac{1}{3L}$ | $a_{17,18}$ | $\omega$ | $b_{16,8}$ | $\frac{\bar{I}_{6q}}{V_{DC2}}$ |
| $a_{7,23}$ | $-(3L)^{-1}$ | $a_{18,2}$ | $(C_1)^{-1}$ | $f_{1,1}$ | $(L_T)^{-1}$ |
| $a_{8,7}$ | $-\omega$ | $a_{18,4}$ | $-(C_1)^{-1}$ | $f_{2,2}$ | $(L_T)^{-1}$ |
| $a_{8,8}$ | $-\frac{R}{L}$ | $a_{18,17}$ | $-\omega$ | $f_{23,3}$ | $\frac{1}{C_4}$ |
| $a_{8,20}$ | $\frac{2}{3L}$ | $a_{19,5}$ | $\frac{1}{C_2}$ | $f_{24,4}$ | $\frac{1}{C_4}$ |
| $a_{8,22}$ | $-\frac{1}{3L}$ | $a_{19,7}$ | $-\frac{1}{C_2}$ | $a_{10,24}$ | $\frac{1}{3L}$ |
| $a_{8,24}$ | $-\frac{1}{3L}$ | $a_{19,20}$ | $\omega$ | $a_{11,11}$ | $-\frac{R_3}{L_3}$ |
| $a_{9,9}$ | $-\frac{R}{L}$ | $a_{20,6}$ | $\frac{1}{C_2}$ | $a_{22,22}$ | $-\omega$ |
| $a_{9,10}$ | $\omega$ | $a_{20,8}$ | $(C_2)^{-1}$ | $a_{22,22}$ | $-(R_{L1}C_3)^{-1}$ |
| $a_{9,19}$ | $\frac{1}{3L}$ | $a_{20,19}$ | $-\omega$ | $a_{10,10}$ | $-\frac{R}{L}$ |
| $a_{9,21}$ | $-\frac{2}{3L}$ | $a_{21,9}$ | $\frac{1}{C_3}$ | $a_{10,20}$ | $\frac{1}{3L}$ |
| $a_{9,23}$ | $\frac{1}{3L}$ | $a_{21,11}$ | $-\frac{1}{C_3}$ | $a_{10,22}$ | $-\frac{2}{3L}$ |
| $a_{10,9}$ | $-\omega$ | $a_{21,21}$ | $-\frac{1}{R_{L1}C_3}$ | $a_{21,22}$ | $\omega$ |
| $a_{22,10}$ | $\frac{1}{C_3}$ | $a_{22,12}$ | $-\frac{1}{C_3}$ | | |

## III.5 Linear Model Validation

In this section, the process of comparing the obtained mathematical model and the actual model is presented. The need for this validation is first discussed and followed the process undertaken and the comparison results are demonstrated.

The accuracy of mathematical models has crucial role in controller development. This is explained by the fact that the controller relies on these mathematical relationships in order to determine the required signal to be sent to the system so that it can achieve a desired equilibrium in the shortest time while satisfying other design specifications. If the mathematical model does not accurately describe the system, the task of controlling a plant may become impossible. It is important; however, to note that there exist more advanced control techniques designed to control systems with uncertainties in their model. This topic is considered to be beyond the scope of this thesis and will therefore not be presented in any further details.

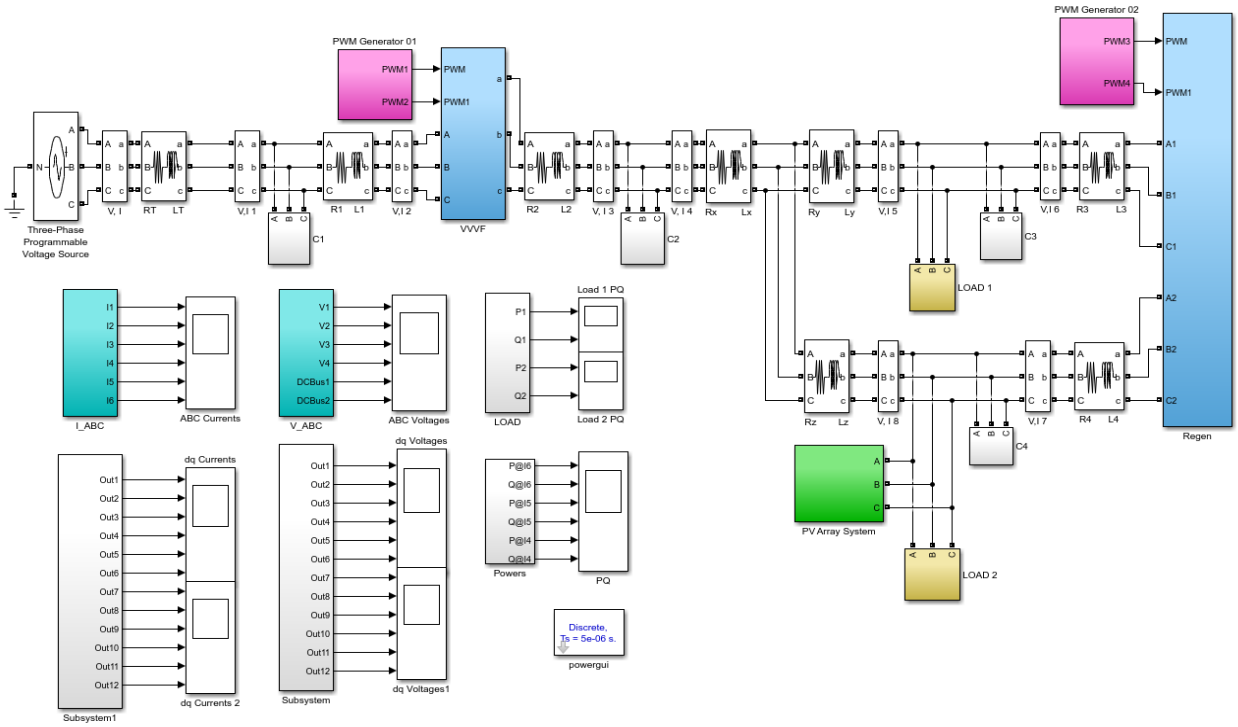


Fig. 12. Actual circuit model as modeled in Matlab/Simulink™.

Having briefly discussed the importance of the need for an accurate model, three specific reasons make it imperative to validate how accurate is the mathematical model derived in this work:

- The first reason is to make the mathematical model matches the physical model. In doing so, it is ensured that this model is reliable and that any controller developed using this system model has a foundation to work with. This is particularly important because other researchers could use this model to develop different control schemes.
- The second reason is to validate the actual modelling technique. There are many ways used to deal with the nonlinearity associated with the control of power electronics. However, the linearization technique used in this work has not been used extensively yet to deal with the nonlinearity associated with power electronics devices.
- Finally, another reason is to check for errors. The likelihood to make mathematical errors increases with the complexity of the modelled system. In this case, checking errors is necessary due to the fact that the derived system model has twenty four equations. Through typing, rearranging and transforming equations into the rotating frame, there is a high chance of making errors. As a result, an independent way to check for any discrepancies is also an objective of this section.

### III.5. a) Validation Process

To ensure that the obtained mathematical model matches the actual one, a comparison of their open-loop responses was used. On one hand, the actual microgrid system was modelled using MATLAB/Simulink™ as shown in Fig. 12. All capacitor voltages and inductor currents of interest are measured, and their respective rotating frame components are computed and plotted in real time so that their dynamics can be evaluated. On the other hand, the same software is used to solve the final system of DEs representing the obtained linear mathematical model for comparison.

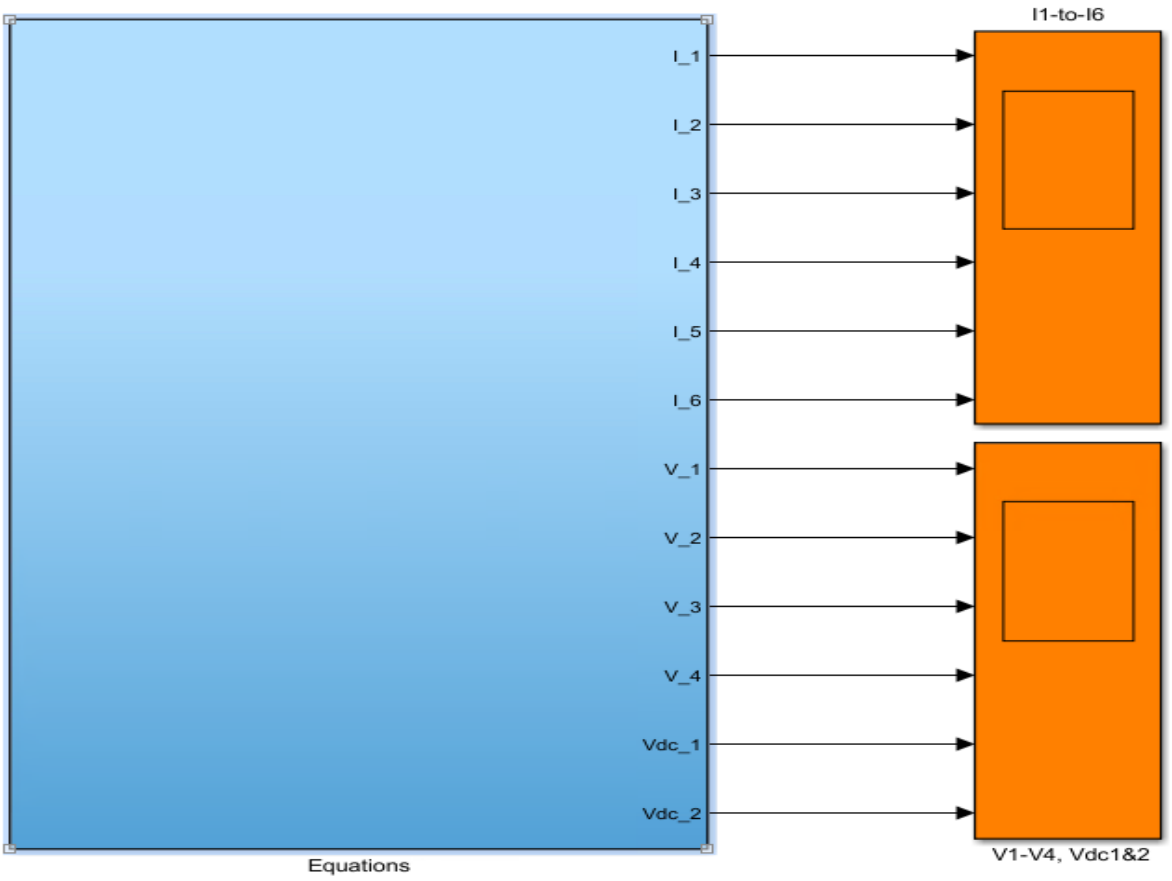


Fig. 13. Mathematical model.

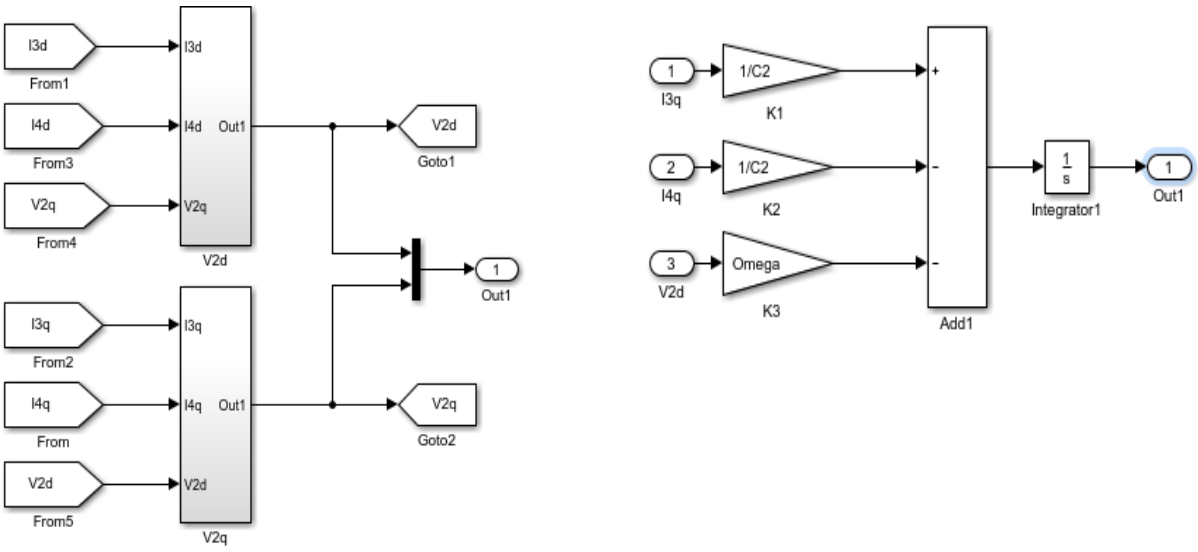


Fig. 14. Mathematical model equations sample.

Fig. 13 and Fig. 14 depict sample MATLAB/Simulink™ blocks used to solve the equations, which represent the mathematical model. Both simulations were run independently and the simulation times were set to be the same in both cases, so that the dynamics of each model can be easily compared.

### III.5. b) Comparison Results

The two models are compared based on two criteria. The first criterion is whether or not both systems have the same dynamics while the second one is to verify if they converge to the same steady state value or not. Inductor currents for the actual model are shown in Fig. 15, and Fig. 17 shows those for the mathematical model. Fig. 16 and Fig. 18 convey the capacitor voltages at different nodes throughout the microgid and the two dc-link capacitor voltages.

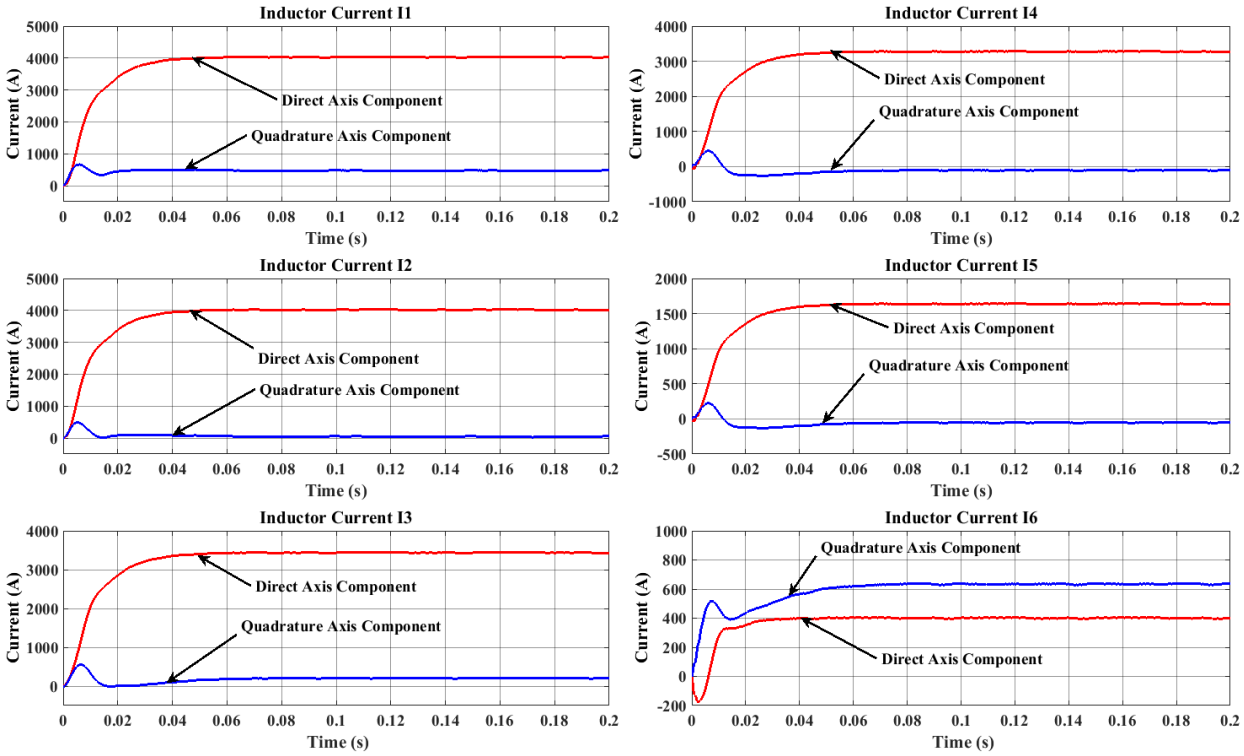


Fig. 15. Filtered inductor currents for the actual circuit model.

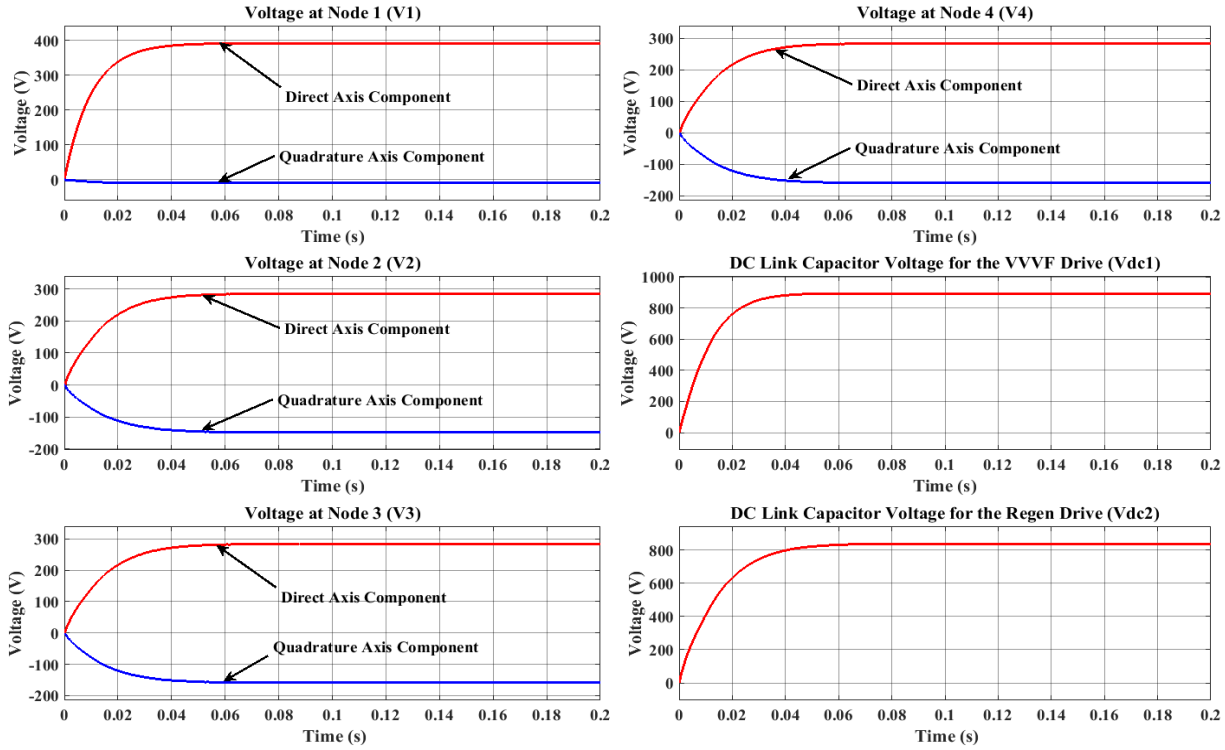


Fig. 16. Filtered capacitor voltages for the actual circuit model.

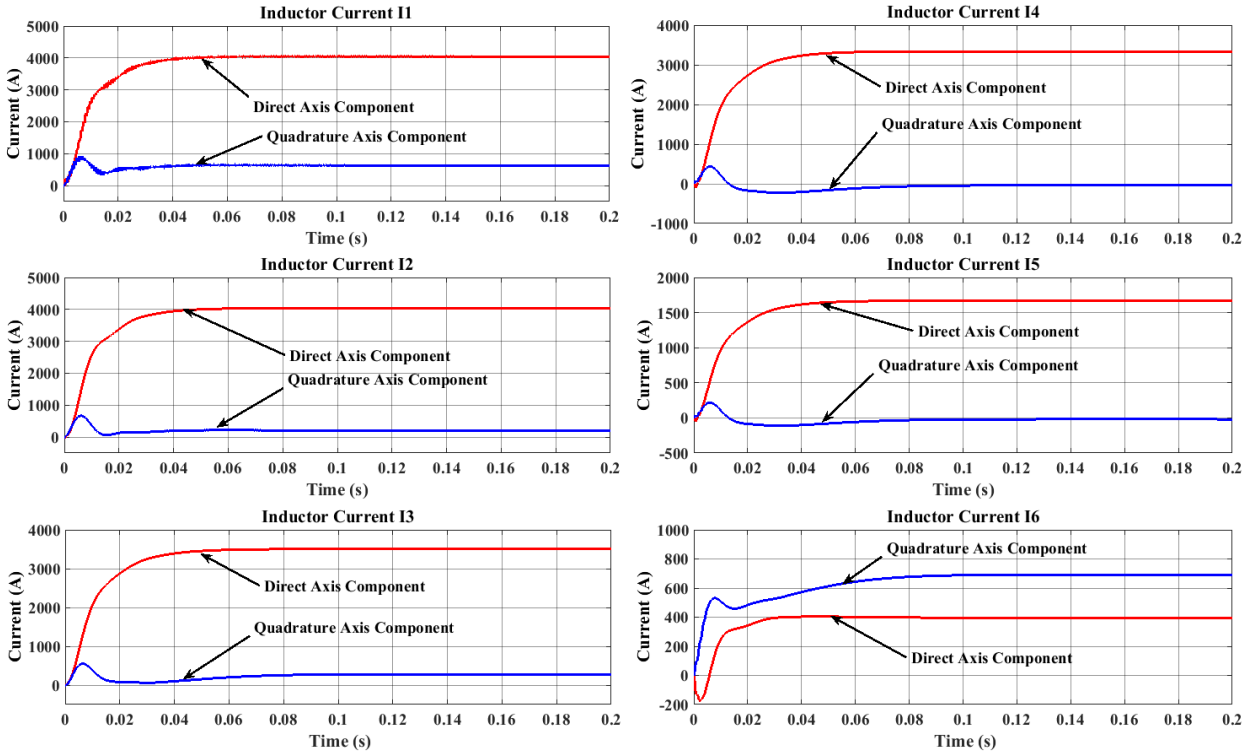


Fig. 17. Filtered inductor currents for the mathematical model.

A comparison of the data shown in Fig. 15 through Fig. 18 shows that the state variables in both models have almost the same state dynamics and nearly converge to the same steady state values. For example, each plot in the inductor currents for the actual model shown in Fig. 15 resembles its counterpart for the mathematical model shown in Fig. 17. The same outcome is observed for voltages in Fig. 16 and Fig. 18, which represent the actual and mathematical models respectively. In order to summarize this comparison between both models, the modulus for each inductor current and capacitor voltage, is calculated using (3.28) and (3.29).

$$\|I\| = \sqrt{{I_d}^2 + {I_q}^2}\ . \tag{3.28}$$

$$\|V\| = \sqrt{{V_d}^2 + {V_q}^2}\ . \tag{3.29}$$

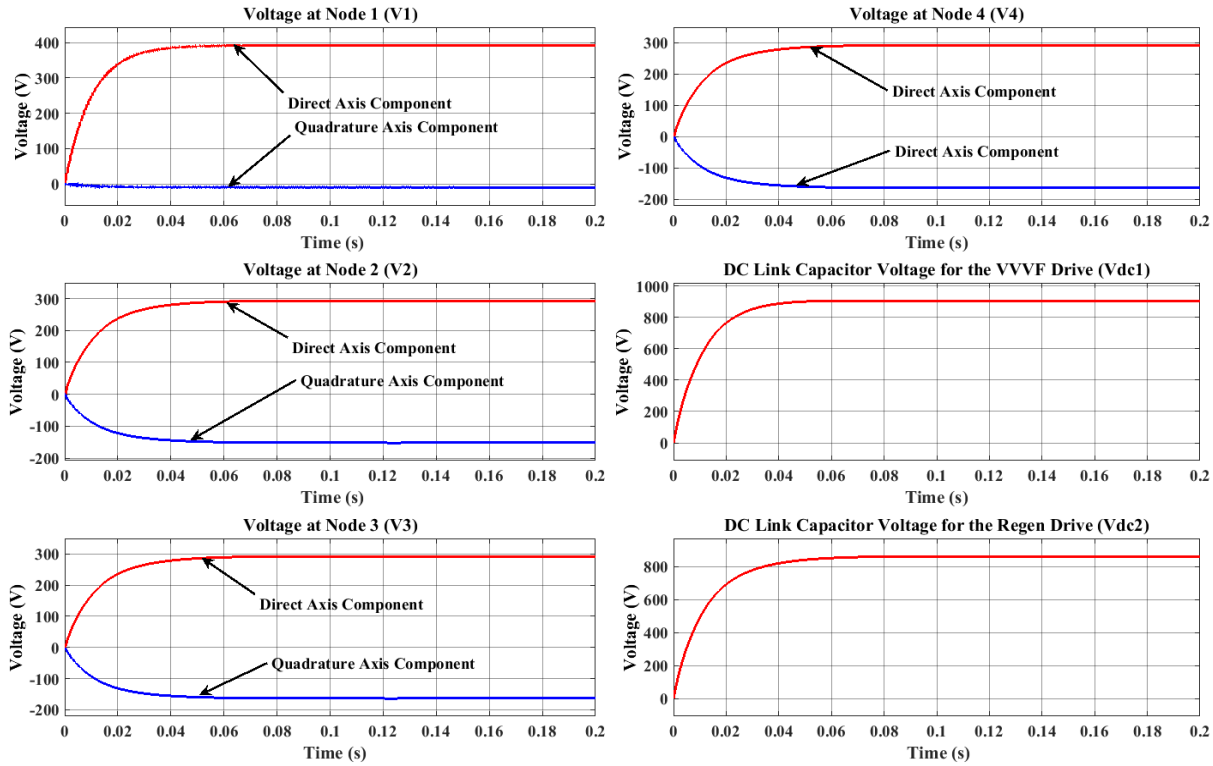


Fig. 18. Filtered capacitor voltages for the mathematical model.

The obtained values are tabulated in Table IV. In addition, the percent error is calculated using formula (3.30) and included in the same table.

$$\% \, Error = \left| \frac{x_{Actual} - x_{Mathematical}}{x_{Mathematical}} \right| \times 100 \, . \tag{3.30}$$

In (3.30), the variable "x" represents either I or V from equations (3.17) and (3.18) respectively. Table IV and Table V facilitate the comparison by compiling the necessary information in one place. The percent error is not expected to be zero because the models do not exactly match. However, the percent error is considerably small and close to zero for almost all state variable. For this reason it can be concluded that both models match without loss of generality.

TABLE IV
COMPARISON BETWEEN ACTUAL AND MATHEMEATICAL MODELS – INDUCTOR CURRENTS

| Sate Variable Modulus | Actual Model Value (A) | Mathematical Model Value (A) | Percent Error Difference (%) |
|---|---|---|---|
| $I_1$ | 4062.06 | 4092.85 | 0.75 |
| $I_2$ | 4023.42 | 4039.86 | 0.41 |
| $I_3$ | 3442.29 | 3516.17 | 2.10 |
| $I_4$ | 3277.62 | 3339.22 | 1.84 |
| $I_5$ | 1638.83 | 1670.11 | 1.87 |
| $I_6$ | 752.71 | 796.43 | 5.49 |

TABLE V
COMPARISON BETWEEN ACTUAL AND MATHEMEATICAL MODELS – CAPACITOR VOLTAGES

| Sate Variable Modulus | Actual Model Value (V) | Mathematical Model Value (V) | Percent Error Difference (%) |
|---|---|---|---|
| $V_1$ | 392.11 | 393.11 | 0.25 |
| $V_2$ | 322.02 | 331.43 | 2.84 |
| $V_3$ | 325.48 | 335.78 | 3.07 |
| $V_4$ | 325.48 | 335.78 | 3.07 |
| $V_{dc1}$ | 873.20 | 910.00 | 4.04 |
| $V_{dc2}$ | 836.50 | 863.00 | 3.07 |

It is important to remember that the mathematical model was linearized around the equilibrium point, but the actual is not linear by nature. Therefore, the actual model can be expected to slightly deviate from this point by a certain margin of error as in fact is the case particularly for $I_6$.

In conclusion, the comparison between the linearized mathematical and actual models show that they both have the same dynamics and converge to the same steady state values with a low percent error. This implies that the obtained linear model can be utilized to develop a linear controller for the actual system. This also means that linearization technique employed could be used, with verification, to linearize a different microgrid system or any other nonlinear system. The root of the percent error is believed to be due to the deviation from the equilibrium point at which the mathematical was linearized by the actual nonlinear model.

# CHAPTER IV SYSTEM POLE-BASED STABILITY ANALYSIS

## IV.1 Introduction

The chapter is intended to investigate the effect of a weak connection between the electric grid and a given microgrid on the stability of the formed system. The microgrid model discussed in the previous chapters will be used as an example, and Fig. 19 shows the topology of this grid-connected microgrid.

Renewable energy resources are increasingly being deployed throughout the electric utility grid [13]. As a result, use of power electronics based power converters as means of interconnection between the different elements of the future grid is projected to increase. However, this interconnection can result in system power flow instability [14]. Likewise, the electrical instability of microgrid systems comprising wind farms and its relationship to the system's parameters are presented in [10]. In this chapter, a similar analysis is perfumed to explore the effect of varying the input impedance on the microgrid system stability.

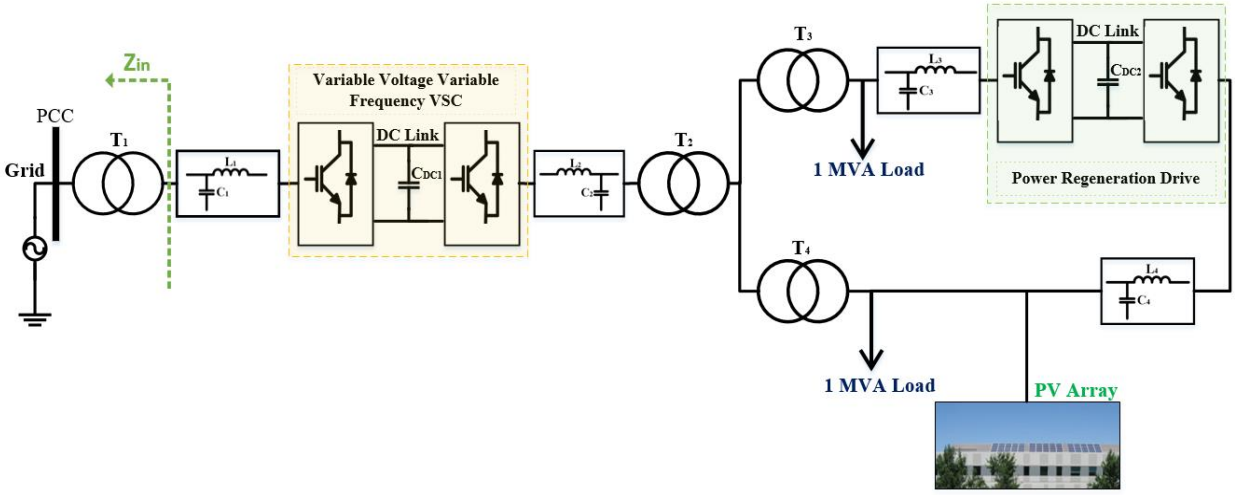


Fig. 19. Microgrid systems - input impedance [27].

The input impedance is shown in Fig. 19 and determines the system's short circuit capacity at the point of interest. This chapter analyzes how input impedance can affect the system stability therefore impacting the size of a microgrid, which can be interfaced at a given electrical node.

## IV.2 A Weakly Connected Microgrid

A weak grid connection can be defined as a situation where the power generated by a wind farm is comparable to the transport power capacity of the power grid to which it is connected [9]. For the scope of this thesis, however, the analysis is based on the variability of the impedance characteristics at the PCC. In fact, the authors [10] argue that there is a correlation between the short circuit magnitude at the PCC in networked voltage systems containing wind farms and the stability thereof. To some degree, the same approach is taken to analyze the stability of the microgrid system shown in Fig. 19.

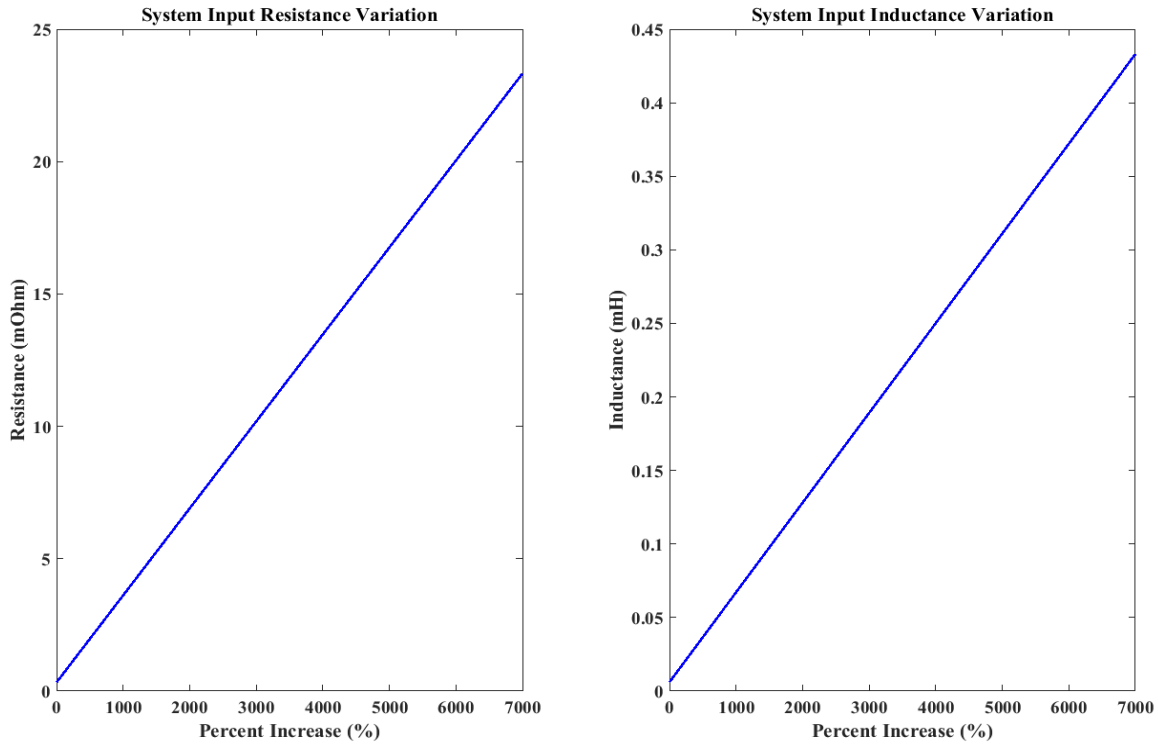


Fig. 20. Input impedance variation range.

## IV.3 Stability Analysis Method

The pole-based stability analysis is used for this analysis. When the overall impedance seen by the microgrid (Zin) is varied over a certain range, the system poles are shifted in the s-plane accordingly. This dependence is due to the fact that the degree to which the microgrid sees the central electric grid as an ideal voltage source changes with the input impedance, Zin. During this study, the input impedance is varied as shown on Fig. 20, and the poles of the system are plotted in the s-plane.

In the complex s-plane, a pole has 2 components: one on the real axis and the other on the imaginary one. When all real axis components are negative the system is stable. The system is said to be unstable if at least one pole has a positive real axis component. It is worth noting that the further to the left the pole's real component (more negative) is, the more stable the system becomes and vice-versa.

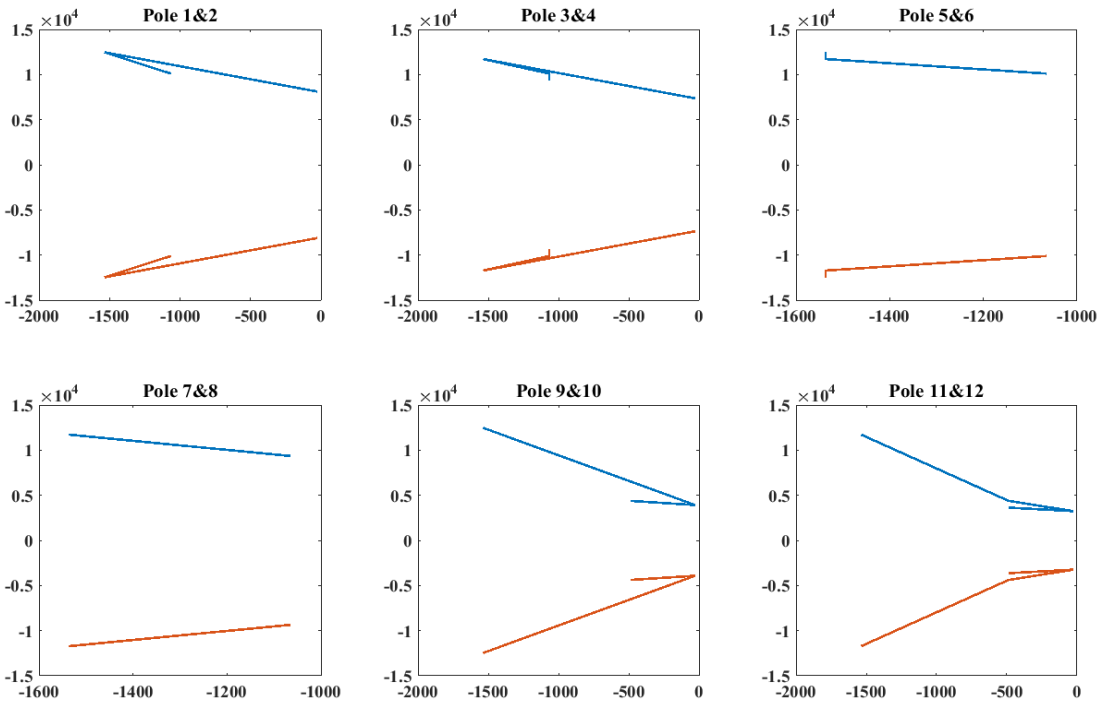


Fig. 21. Change in eigenvalues with variation of input impedance.

Marginal stability is used to refer to the case when at least one of the pole has a zero real part. Finally, the imaginary component indicates the frequency of oscillation of the associated system state. Thus, it is less considered for this analysis.

The effect of varying the system input impedance on the system poles is illustrated by the shift in pole locations as Fig. 21 and Fig. 22 show. Each subplot portrays the variation of the pole location for a given system state (capacitor voltage or inductor current). As indicated in the graphs, most of the poles approach zero when the input impedance increases. This implies that electrical connection weakens as this input impedance rises.

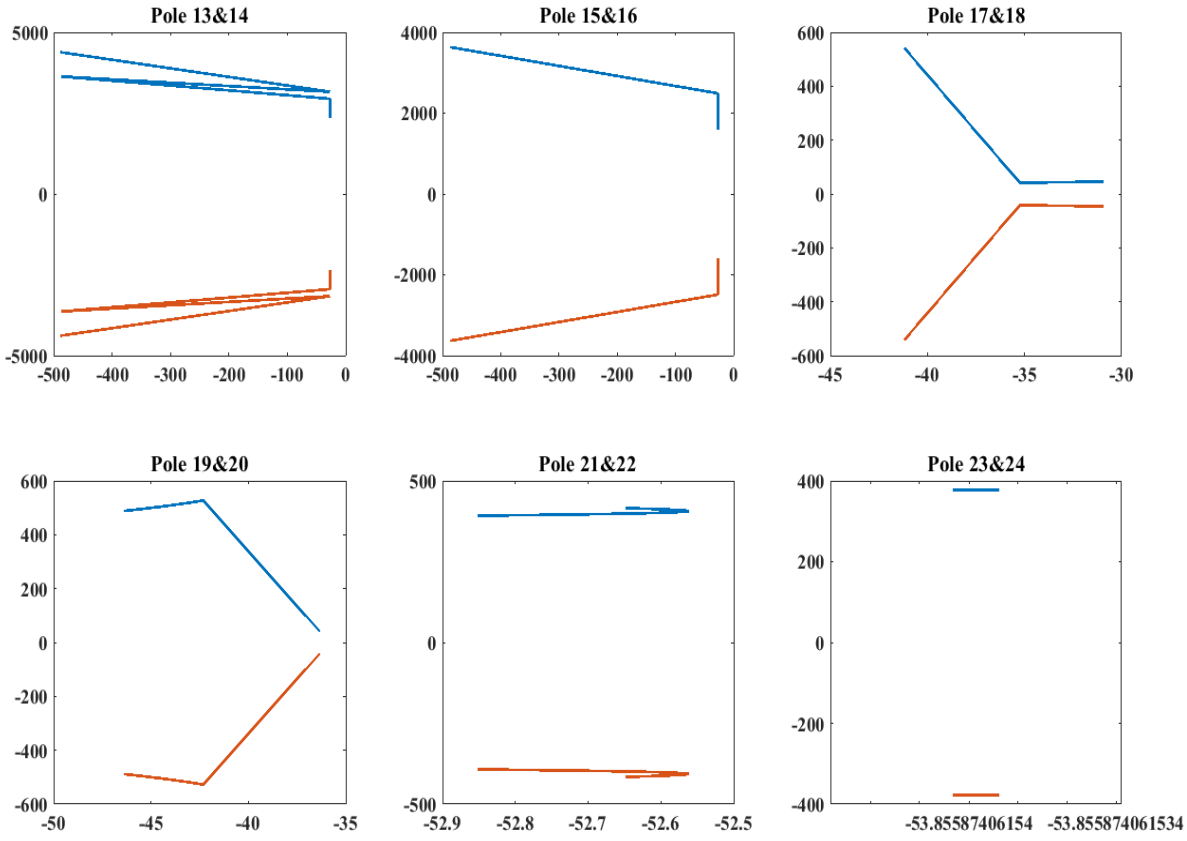


Fig. 22. Change in eigenvalues with variation of input impedance (Cont.).

## IV.4 Stability Analysis Implications and Potential Benefits

Dynamic stability analysis is one of the most important and effective elements for greater security and reliability of planning, design, operation and economic aspects of electric power network [16]. This type of analysis can be beneficial in many applications including but not limited to:

- Designing advanced control schemes for a stable operation of grid-connected distributed energy resources (such as solar, wind, etc…). This is because a deep understanding and analysis of stability margin is needed to design a robust controller.
- Power system planning engineers who must determine optimal locations where renewable energy resources can be interfaced with the existing electrical grid without jeopardizing it reliability.
- Determining the generation capacity limit of a microgrid depending on its locations in relation to the electric grid.

# CHAPTER V LINEAR QUADRATIC OPTIMAL CONTROLLER DESIGN

## V.1 Introduction

This chapter briefly introduces the reader to the optimal control theory for the proposed linear quadratic optimal controller. The theoretical background is revisited to better clarify the motivation, and the appreciation for optimal control theory. A solution to the optimal control problem, the linear quadratic regulator (LQR), is discussed. Also, the Matlab/Simulink™ implementation of the proposed control scheme is presented to elaborate the process undertaken to get the results presented in chapter VI. Moreover, the multiple inputs multiple outputs (MIMO) systems, and the transfer functions for MIMO systems are introduced towards the end of the chapter.

## V.2 Linear Quadratic Optimal Control

The linear quadratic optimal control problem seeks to stabilize a system while minimizing the associated cost function [17], [23]. Otherwise stated, this control technique reduces the magnitude of the cost function associated with the controller while improving the system's response to a stimulus. In linear quadratic optimal control literature such as in [23], the cost function is usually defined by equation (5.1) as

$$J = \int_0^\infty [x^T(t)\, Qx(t) + u^T(t)\, Rx(t)]\, dt \tag{5.1}$$

with the matrix Q being symmetric, semidefinite and positive, and R is a positive, symmetric, and definite matrix.

The LQR controller is a solution to the optimal control problem where a full state feedback is assumed, and the disturbance input is considered to be zero. With this assumption, an optimal state feedback law $u(t) = K(t)$, which corresponds to the minimum solution to the cost function

(5.1) is obtained. In this static state-feedback controller, the matrix *K* is determined using (5.2) in which *P* constitutes the distinct definite and positive solution to Algebraic Riccati equation (ARE) given in (5.3). In the last-mentioned equation, variables are matrices. Another way to calculate the matrix *K* is to use the Matlab/Simulink™ function, lqr().

$$K = R^{-1}B^T P\,. \tag{5.2}$$

$$A^T P + PA - PBR^{-1}B^T P + Q = 0\,. \tag{5.3}$$

Fig. 23 shows the implementation of an LQR for a system having all states available for measurements.

In practice however, all states might not be available for measurements or one might need to reduce the number of sensors. In such a case, a linear quadratic Gaussian (LQG) or Kalman filter state estimator (LQE) can be used to estimate the states. The estimated states are those, which are not available for measurements from the system's input and output according to linear states observer equation (5.4) [23].

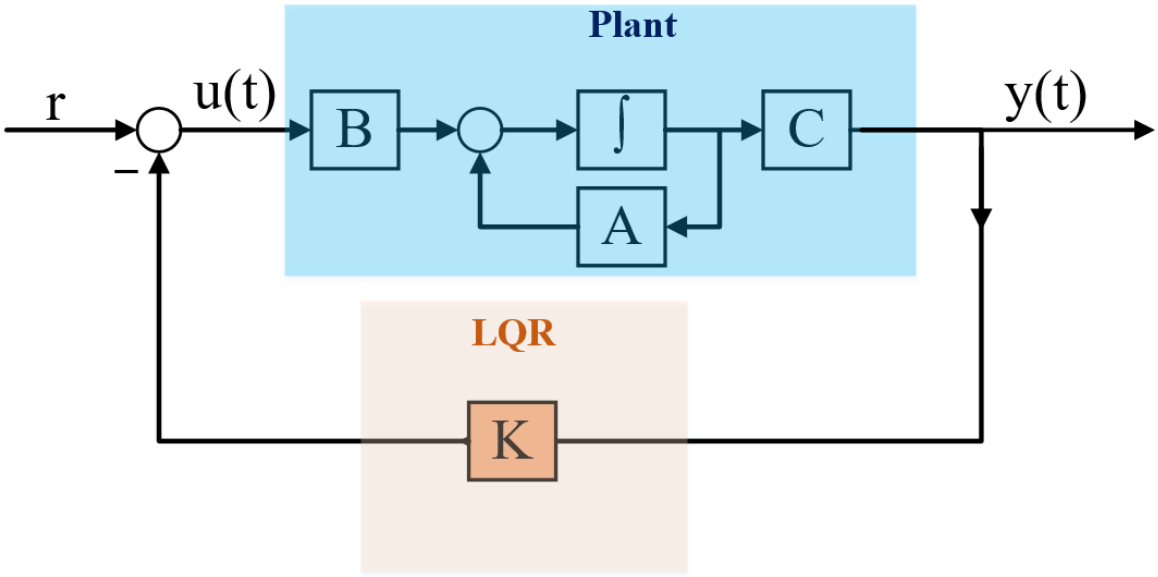


Fig. 23. LQR for a system with all states available for measurement.

$$\frac{d\hat{x}}{dt} = A\hat{x}(t) + Bu(t) + L[y(t) - \hat{y}(t)]\,. \tag{5.4}$$

In (5.4), the optimal estimator gain L is given by equation (5.5) in and P is the unique matrix solution to ARE in (5.6).

$$L = PC^T V^{-1}\,. \tag{5.5}$$

$$AP + PA^T - PC^T V^{-1} CP + W = 0\,. \tag{5.6}$$

For a general case where only certain states are available for measurement, both the LQE and the LQR can be used to stabilize a control system in the optimal sense. A typical implementation of such a controller is shown in Fig. 24. It is important to mention that the integral term is often used to help drive the error between the reference input and the desired output to zero quickly. In such a case, the error signal results in system states augmentation by one or more states depending on the designer's choice and the number of inputs and outputs of available. This state augmentation results in a controller configuration shown in Fig. 25.

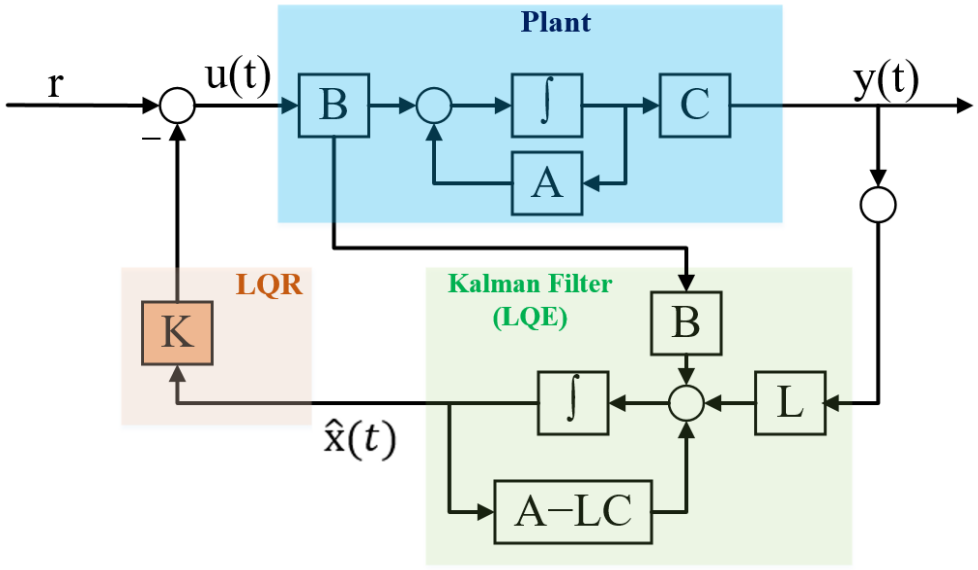


Fig. 24. Implementation of an LQR with a Kalman filter.

## V.3 Implementation in Matlab/Simulink™

The microgrid system presented in this work constitutes a multiple inputs multiple outputs (MIMO) system from a control perspective. MIMO systems are well known and have been extensively covered in modern control textbooks as in [23]. Fig. 26 illustrates the microgrid as MIMO system.

Revisiting the mathematical model obtained in Chapter III, the system dynamics are represented by the following system of equations

$$\begin{cases} \dot{x} = Ax + Bu + Fu_d \\ y = Cx \end{cases} \qquad with\ x \in \mathbb{R}^n, u \in \mathbb{R}^p, u_d \in \mathbb{R}^m\ and\ y \in \mathbb{R}^q \qquad (5.7)$$

where $x$ represents the state variable, $u$ denotes the controlled-input, $u_d$ is the disturbance input matrix and $y$ is the output vectors. The matrices $A$, $B$, $F$ and $C$ are the non-constant respective matrices of appropriate sizes with the notation of [23] adopted.

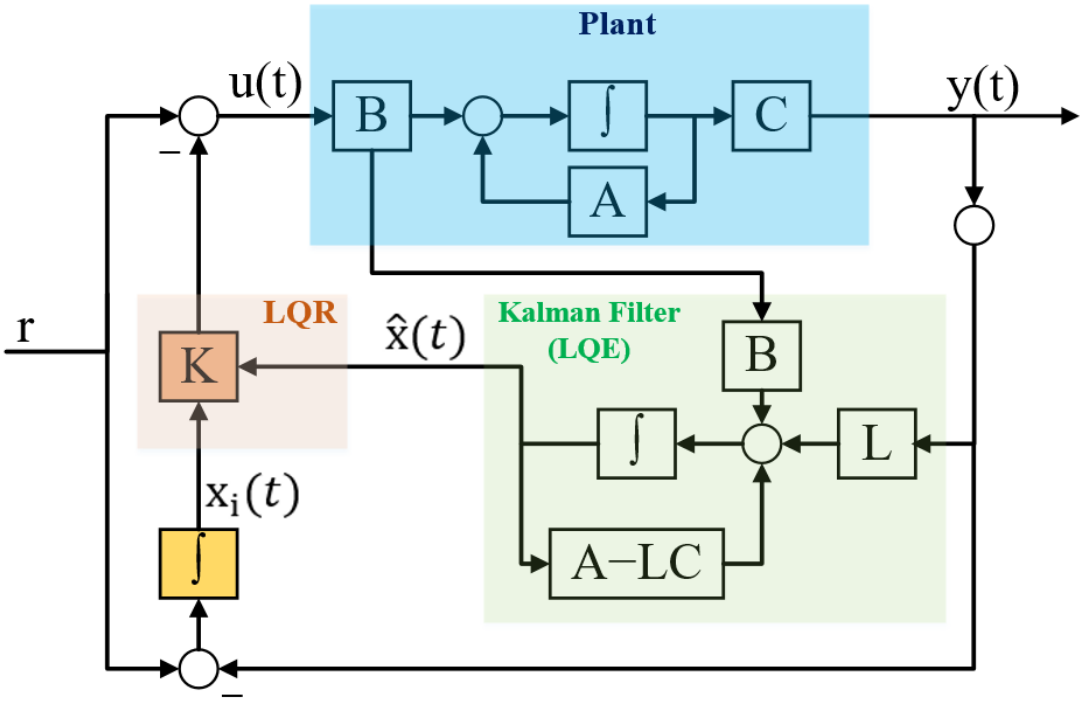


Fig. 25. Implementation of an LQR with a Kalman filter and integral of the error.

Let **Y**(s) and **U**(s) be the Laplace transform of **y** and **u** respectively, and assume the absence of the disturbance input. The system can be represented using (5.8) in which the input is directly related to the output.

$$\boldsymbol{Y}(s) = \boldsymbol{G}(s)\boldsymbol{U}(s) \tag{5.8}$$

The matric G(s) is the transfer matrix of dimension h × p. With h being the number of outputs and p is the number of inputs such that

$$\mathbf{G}(\mathrm{s}) = \begin{bmatrix} \mathrm{G(s)}_{1,1} & \cdots & \mathrm{G(s)}_{1,\mathrm{p}} \\ \vdots & \ddots & \vdots \\ \mathrm{G(s)}_{\mathrm{q},1} & \cdots & \mathrm{G(s)}_{\mathrm{q,p}} \end{bmatrix} \tag{5.9}$$

From equations (5.8) and (5.9), the relationship between a given input and output can be deduced to obtain (5.10).

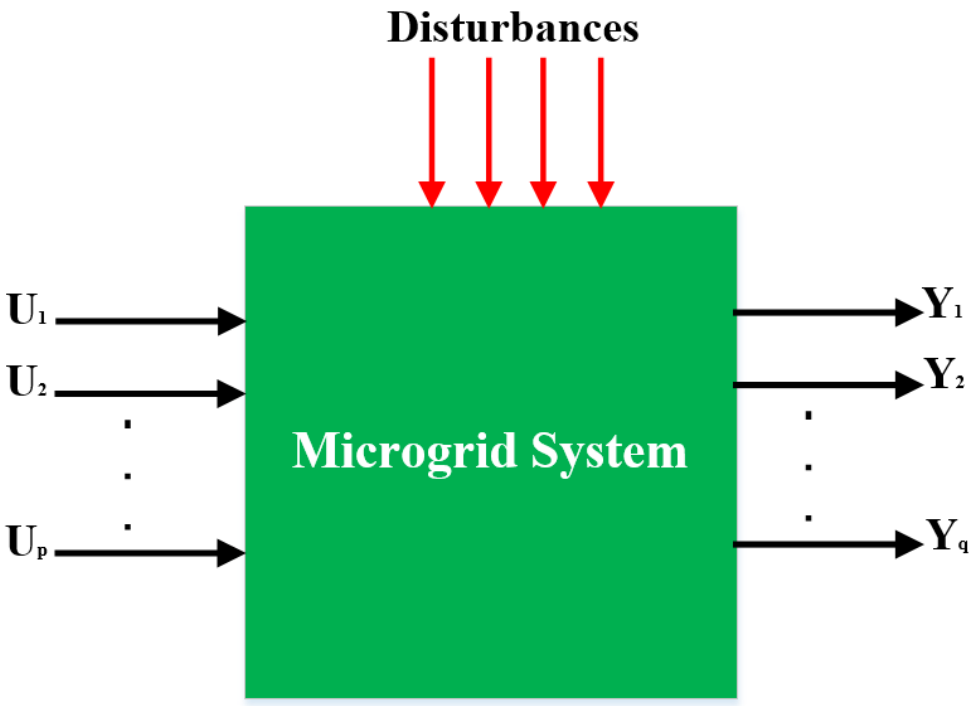


Fig. 26. MIMO system representation of the microgrid system.

$$\mathrm{Y(s)_i} = \mathrm{G(s)}_{ij}\mathrm{U(s)_j}\,. \tag{5.10}$$

With $i = [1, \ldots, q]$ and $j = [1, \ldots, p]$. Sample transfer functions relating obtained using is provided in Appendix B. The input-output relationship for the system can then be calculated using equation (5.11) as follows:

$$\mathrm{Y(s)_i} = \mathrm{G(s)}_{i1}\mathrm{U(s)}_1 + \mathrm{G(s)}_{i2}\mathrm{U(s)}_2 + \cdots + \mathrm{G(s)}_{ip}\mathrm{U(s)_p}\,. \tag{5.11}$$

The Matlab/Simulink™ tf() command was used to convert the space-model in (5.7) to the transfer matrix of (5.9). The step response can then be plotted using the Matlab/Simulink™ step() command.

The mathematical derivations, which are briefly presented in this chapter were used to design the proposed LQR controller for the microgrid system covered by this work. Moreover, the controller was implemented using Matlab/Simulink™, and the obtained results are covered in the following chapter.

# CHAPTER VI SIMULATION RESULTS AND ANALYSIS

## VI.1 Introduction

This chapter presents the results obtained by implementing the optimal LQR controller designed in Chapter V on the microgrid system explained in previous chapters. By means of plots, the system's response to a step change in input is demonstrated for selected state variables. The performance of the proposed controller is compared to that of a proportional plus integral (PI) one. Finally, an analysis of the obtained results concludes this chapter.

## VI.2 The Controlled Systems and Output States Selection

The controlled system has twenty-four state variables, but only six of them are chosen as the system output. This choice is solely based on brevity and the significance of the selected states. The output is comprised of the two dc-link voltages for the VVVF and Regen converters and the two load voltages. The results consist of the step responses of the selected states to a step change in switching functions. Each load voltage accounts for two state variables because the model is in the synchronous rotating frame. This means that there are two components, a direct axis and a quadrature axis, for each load voltage.

Throughout the results presented in this chapter, the performance of the proposed control scheme proves to be particularly effective in bringing the state to its steady state value within a short rising time and zero percent overshoot. For each state, both a step response with an LQR controller and that with a PI controller are provided for comparison. It is seen that the optimal LQR outperforms the conventional PI controller. The following six states are chosen as output of the controlled system: the dc-link capacitor voltages for the VVVF and the Regen drives respectively, and direct axis and quadrature axis components for each of the two load voltages.

The first reason for the above choice is that the power flow must maintain a balanced state, and the back-to-back dc-link voltage regulation is crucial for this equilibrium [18]. As a result, for either active power conditioner (APC) in the microgrid system in Fig. 27, the dc-link voltage is chosen as a system output. Also, there is always a trend to decrease the cost associated with the dc-link capacitor usually by making it smaller. However, if the reduction of the dc-link capacitor is sought after, then the requirement for a fast control is needed accordingly [19]. These are some of the many reasons why dc-link regulation is always a concern in power converters control and operation. These reasons, too, explain why the dc-link voltages were chosen in this chapter, to discuss the performance of an LQR controller. It is observed that the last-mentioned controller has a fast response that can also be used in dc-link capacitor minimization presented in [19].

In addition, the control objectives should keep in line with any standards applicable for the controlled system. For example, the American National Standard Institute (ANSI) defines voltage levels and voltage ranges in its ANSI C84.1 section to limit how much the load voltage should deviate from the nominal value.

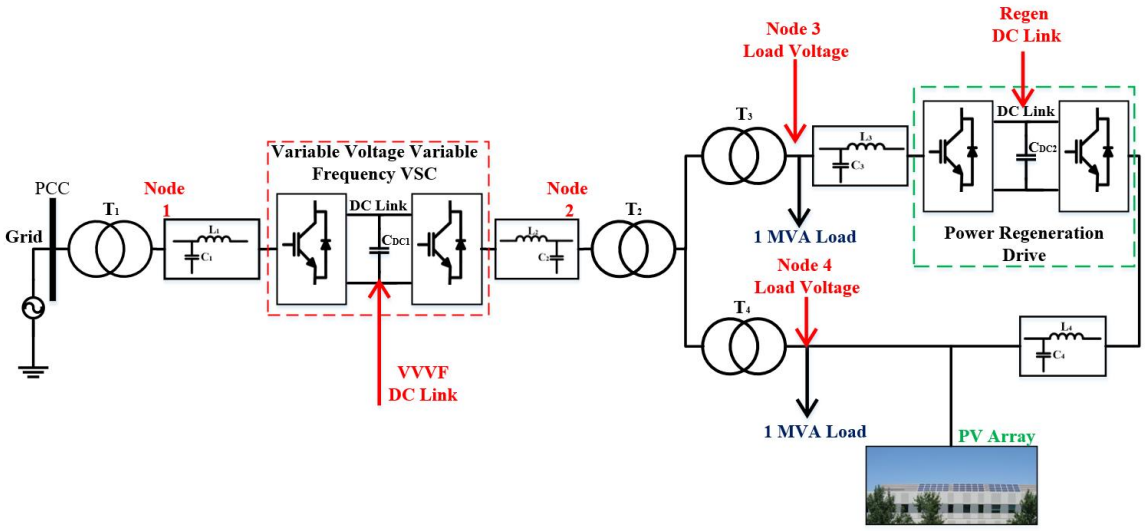


Fig. 27. Arbitrary nodes used to states presented in this chapter.

ANSI C84.1 sets the service voltage to stay within a ±5% margin that is a minimum of 95% and a maximum of 105% of the nominal voltage for its preferred range commonly known as Range A. This standard applies to 120V- 600V systems; the microgrid covered in this thesis is a 480V line-to-line system. ANSI C84.1 standards cover more than what is mentioned above, but the point being made here is to ensure that the load voltage reaches its steady state value within its acceptable range in a short time as the controller brings the system to its steady state in response to a given scenario. There are numerous causes that can trigger the controller action. For instance powering a large motor is a common reason that momentarily affects the system's voltage. Also, losing one of the voltage sources that feed the microgrid system can be another reason. This is why the load voltages were utilized to show the efficacy of the proposed control scheme.

### VI.3 Results

It was previously introduced that the system's input matrix has eight elements, and change in a given input has a specific effect on a certain output as determined by a characteristic transfer function. System transfer functions are discussed in chapter V and formula (5.10) explicitly shows this mathematical relationship between an input and an output. Moreover, the transfer functions specific to this work were calculated using Matlab/Simulink™, and appendix B provides a few samples. These transfer functions were used to obtain the results covered in this section, which are step responses to a step input to the system.

Fig. 28 shows the step responses of the VVVF drive dc-link voltage (top) and that of the regen drive (bottom) to a step change of the switching functions. The dashed blue plot is the step response obtained when a PI controller is employed while the solid red plot results from using an LQR one. It is observed that for the proposed LQR controller, the step response reaches 90 percent of the steady state value in about 10 milliseconds.

This performance index is known as the rise time and measures how fast the controller responds to a system input. Also, the voltage percent overshoot is zero for this controller, which indicates that the response does not exceed the steady state final value. Furthermore, the settling time, which indicates how fast the response reaches and stays within 2 percent of the final value, is 18 milliseconds for the proposed LQR controller.

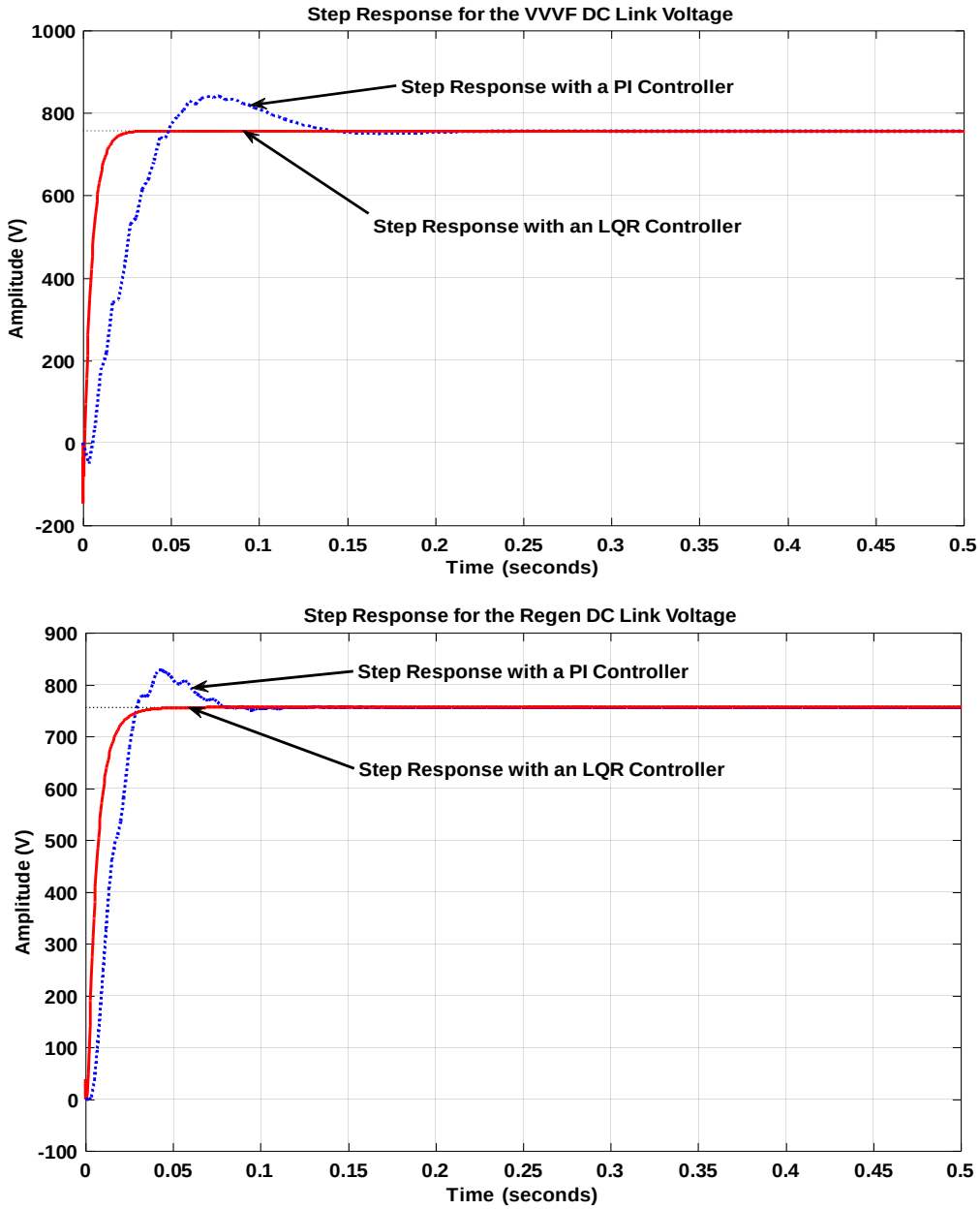


Fig. 28. Step response of dc-link voltages: VVVF (top) and regen drive (bottom).

In comparison with the LQR controller, it is observed that the PI controller resulted in a slower response with a 10 percent overshoot. In fact, for the $V_{dc1}$, a 32 milliseconds rise time and a 124 settling time are obtained when a PI controller is used. Nearly the same results are obtained for $V_{dc2}$ with the exception that the rising time is reduced to 19 milliseconds and the settling time lowered to 73 milliseconds for a PI controller.

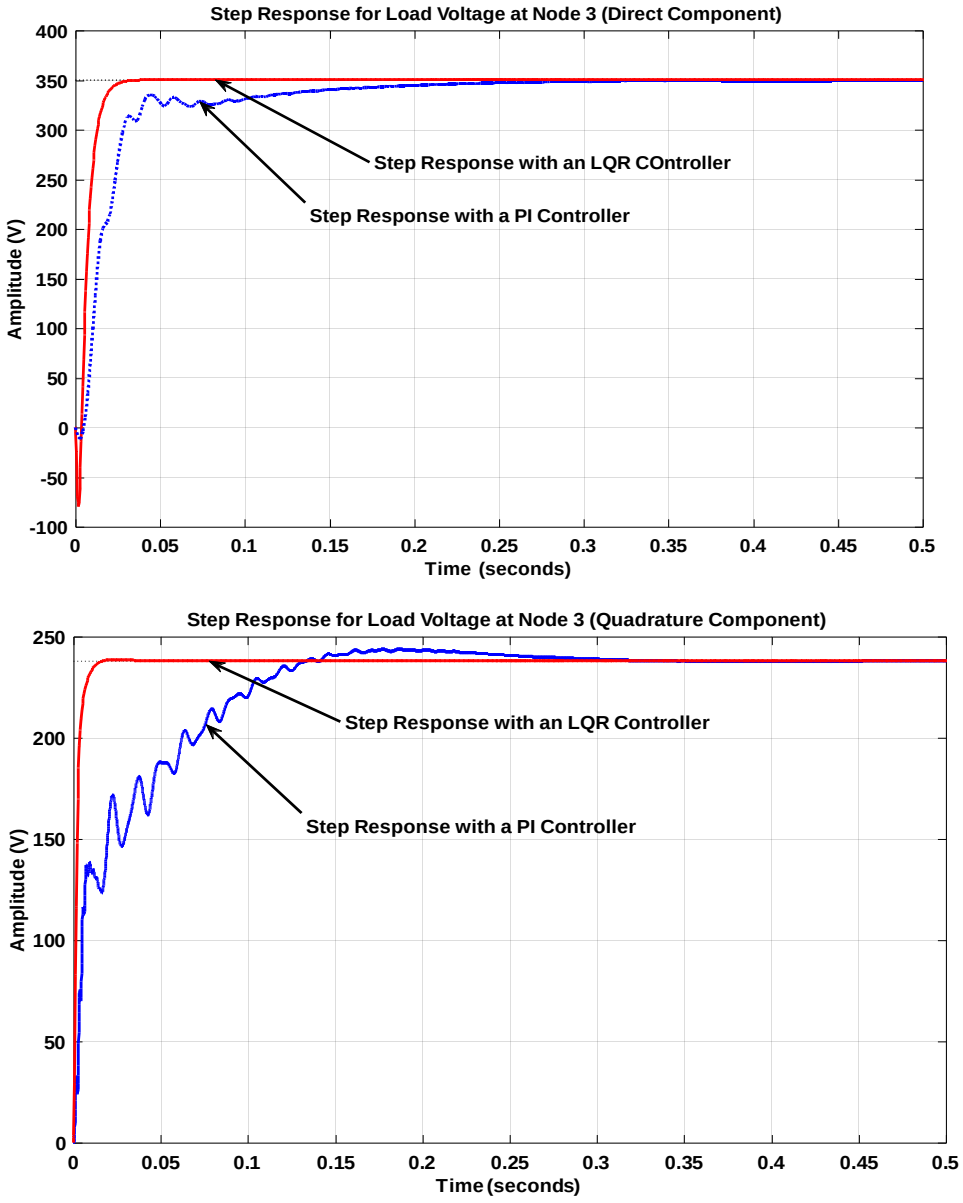


Fig. 29. Step response for load voltage at node 3: direct axis (top) and quadrature axis (bottom).

The rest of the performance characteristics remain almost the same for both controllers of the two dc-link voltages.

In Fig. 29, the step responses for the load voltage at node 3 are shown with the direct axis component on the top graph and the quadrature axis component on the bottom one. Likewise, the dashed blue plot is the step response obtained when a PI controller is employed while the solid red plot results from using an LQR one. It is noticed that the difference between the step responses for the voltages at node 3 and those for the dc-link voltages is that there is a particularly low overshoot for both controller schemes in the former case. For the LQR controller, the direct axis component exhibits a zero percent overshoot and the quadrature axis one a 0.24 percent overshoot. For the PI controller, the direct axis component does not exceed its final value while the quadrature axis one overshoots with only 2.5 percent. However, both the rising and settling times observed for the voltage at node 3 indicate the same dissimilarities between the controllers as do the step responses for the dc-link voltages. For example, the quadrature axis voltage component has a 173 milliseconds settling time for a PI controller while it only has 21 milliseconds with an LQR controller. These results continuously emphasize that the proposed LQR controller is faster and more effective than its PI coequal.

Fig. 30 shows the step responses for the load voltage at node 4. The direct axis component is shown on the top and the quadrature axis component on the bottom of the Fig. 30. The step response obtained with a PI controller is shown by the dashed blue plot while that resulting from use of an LQR one is shown in solid red plot. It is clearly seen that the performance characteristics are identical to those observed for the load voltage at node 3. For this reason, they are not repeated to avoid redundancy. However, it is important to note any arguments, which explain this similarity. One of the plausible explanations for this homogeneity is the symmetry of the microgrid system of Fig. 26. As shown in the last-mentioned figure, both loads are located at the ring-type

configuration of the microgrid. The two load voltages are expected to have the same dynamics because the LC-filters 3 and 4 are identical, and the transformers T3 and T4 are similar. This assumption may not hold true for the case when only the PV array is supplying the voltage, but it still helps to explain why both load voltages have the same behavior.

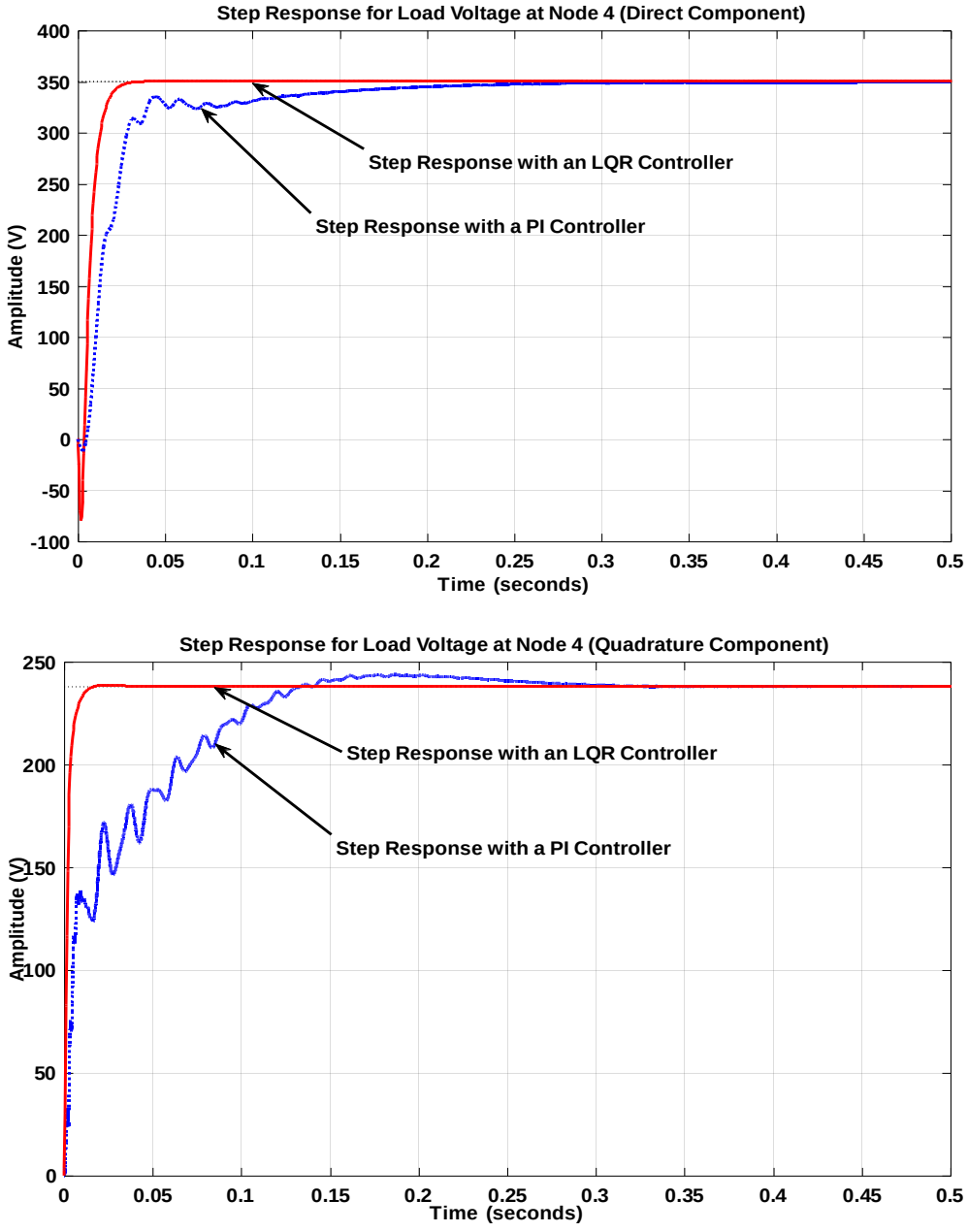


Fig. 30. Step response for load voltage at node 4: direct axis (top) and quadrature axis (bottom).

To summarize the results, Table VI provides the average performance characteristics of each controller. The average is based on the results presented in this section. In terms of the rising time, the proposed LQR controller outperforms its PI counterpart by a factor of 5.3 on average. Table VII also indicates that the LQR controller offers a settling time, which is about 10 times better than that resulting from using a PI controller. Finally, the overshoot associated with using an LQR controller is 50 times smaller than that observed with a non-networked PI controller.

### VI.3 Results Analysis

The often-desired outcome in many control applications is for the closed-loop output to optimally track a given trajectory with minimal error and at the lowest possible cost [20]. This optimization is usually the goal in virtually all areas where control theory is applied including but not limited to aerospace, energy, manufacturing and medicine [20]. In addition, it is always desired that a controller's action on a given plant results in the fastest attainable response with minimum overshoot. As a result of the controller's performance enhancement, the system's resilience improves.

As the trend towards a highly interconnected smart electric grid gets more favorable, extra renewable resources will be added especially at the distribution level. That being the case, control will keep to play a vital role in maintaining the stability of modern interconnected power systems [21]. The proposed LQR controller offers improved performance in comparison to the often-used PI controller as shown in the results.

TABLE VI
CONTROLLER PERFORMANCE COMPARISON

| Controller | Rising Time (s) | Settling Time (s) | Percent Overshoot (%) |
|---|---|---|---|
| LQR | 8.333E-03 | 1.750E-02 | 0.48 |
| PI | 4.433E-02 | 1.615E-01 | 25.6 |

This implies that some operational challenges might be mitigated when an LQR controller is used as a substitute for its PI counterpart. Furthermore, this stability improvement suggests the ability to include larger generation capacities to microgrid systems.

# CHAPTER VII CONCLUSIONS AND FUTURE WORK

## VII.1 Introduction

In this chapter, the thesis' objectives are revisited in order to better present major conclusions drawn from the results of different studies contained herein. Through these conclusions, the author points out what he believes the results obtained can contribute to on-going grid improvement. Future works in support of this contribution are suggested.

The electric grid continues to undergo new changes, which challenge its traditional and unidirectional operation. This has attracted efforts to apply advanced control theories to the stabilization of microgrids and the integration of renewable resources [18, 19, 20, and 21]. Moreover, system analysis and simulation methods need to continuously be revised and improved for robust and cost-effective operation of the electric grid. [21]. In light of this trend, the main objective of this thesis is to design a linear quadratic regulator (LQR) optimal controller for a cascaded inverters-based microgrid system. In order to accomplish this task, three sub-objectives are identified in chapter I as follows:

1. Develop an accurate mathematical model, which represents a physical system and matches the simulation model. This ensures that the developed controller reflects the dynamics of the system and controls a realistic, accurate system model. In addition, the developed model can be used for other research initiatives and analysis.

2. Perform a stability analysis of the system to determine some of the factors that can affect its stability margin. The effect of the change of the input impedance on the system's stability is analyzed.

3. Design an LQG optimal controller to improve the system's stability margin and analyze its performance in that regard.

## VII.2 Conclusions

In chapter three, a non-linear mathematical model was derived for the microgrid system using Kirkoff's current and voltage laws. The twenty-four differential equations obtained constitute this non-linear model and represent the physical microgrid, which is presented in chapter II. To overcome the inherent nonlinearity due to switching of power electronics devices, a linearization technique using Taylor series expansion is proposed and applied in chapter III. The obtained linear model was validated for accuracy in the same chapter. It is shown that both the linear mathematical model and the Matlab/Simulink$^{TM}$ one, which represents the physical model, converge to the same values. Not only did they converge to the same values, but they also have the same dynamics as presented in chapter III. The results of this independent model validation suggest that the obtained linear representation can be reliable for controller development. They, in return, prove that the linearization technique can indeed be used to linearize non-linear models.

In chapter IV, the pole-based stability analysis of the microgrid system is evaluated to study how the system stability margin is affected by the change in input impedance. It was observed that as the input impedance increases, the real parts of the system poles move toward zero, which suggests a reduction in system stability. The author believes that this kind of analysis has potential benefits as follows:

- Designing advanced control schemes for a stable operation of grid-connected distributed energy resources (such as solar, wind, etc...). In this application, a deep understanding and analysis of stability margin is essential to robust designs.

- Power system planning for engineers who must determine optimal locations where renewable energy resources can be interfaced with the existing electrical grid while keeping its reliability intact.
- Determining the generation capacity limits for a microgrid based on its location in relation to the electric grid.

Finally, in chapter V the proposed optimal LQR controller was designed and implemented for the linear model. Also, the background of the proposed control scheme in terms of the cost function minimization is presented, and the advantages of this optimization leading to a robust controller are discussed. Additionally, the Matlab/Simulink$^{TM}$ implementation of the proposed controller is covered in the mentioned chapter.

The obtained results are presented in chapter VI. A comparison with the results obtained using a non-networked PI controller shows that the proposed LQR offers great improvements. It can be concluded that as the number of distributed resources seen by the electrical grid continues to rise, some operational challenges might be mitigated by using an LQR controller in place of its PI counterpart. Furthermore, the proposed controller enhances the stability of the system, which means that larger generation capacity is attained.

### VII.3 Future Work

There are numerous activities that can be undertaken to further the work presented in this thesis to a higher level in terms of applicability and usefulness. Likewise, more work can be accomplished to validate and further explore the scope of this contribution and how to widen it for microgrid applications. The suggested ideas include but are not limited to:

- ⇨ Distributed controllers could be considered in spite of the proposed central one. This would reduce the complexity in the developed model as each local controller can regulate a well-defined subsystem and share information with other controllers.
- ⇨ A linear quadratic estimator (LQE), also known as a Kalman Filter, could be explored for systems modeled using the same linearization technique presented in this work. The benefits of this control scheme include alleviating uncertainties in developed models due to linearization as well as those due to actual parameter value measurements.
- ⇨ Finally for stability analysis, more advanced methods such as the relative gain array can be explored to analyze the effect of input impedance on the overall stability of the system.

## REFERENCES


[1] G. Strbac, N. Hatziargyriou, J. P. Carvallo Lopes, C. Moreira, A. Dimeas, and D. Papadashalopoulos, “Microgrid: Enhancing the resilience of the European megagrid,” in *IEEE Power Energy Mag.,* vol. 13, no. 3, pp. 35–43, May–Jun. 2015.

[2] T. Ise, Y. Hayashi, and K. Tsuji, “Definition of power quality levels and the simplest approach for unbundled power quality services,” in *Harmonics and Quality of Power, 2000. Proc. 9th Int. Conf.*, vol. 2, pp 385–390, 2000.

[3] H. Farhangi, “The path of the smart grid,” in *IEEE Power & Energy Magazine,* vol. 8, no. 1, pp. 18–28, Jan-Feb. 2010.

[4] X. Tang, W. Deng, and Z. Qi, “Investigation of the dynamic stability of microgrid,” in *IEEE Trans. Power Sys.*, vol. 29, no.2, pp. 698–706, Mar.2014.

[5] Q. Fu, L. F. Montoya, A. Solanki, A. Nasiri, V. Bhavaraju, T. Abdallah, and D. C. Yu, “Microgrid generation capacity design with renewable and energy storage addressing power quality and surety,” in *IEEE Trans. Smart Grid*, vol. 3, pp. 2019–2027, 2012.

[6] A. B. M. Nasiruzzaman and H. R. Pota, “A new model of centrality measure based on bidirectional power flow for smart and bulk power transmission grid,” in *EEEIC 2012.*, pp.1−6, May 2012.

[6] M. Reza, D. Sudarmadi, F.A. Viawan, W.L. Kling, and L. Van Der Sluis, "Dynamic Stability of Power Systems with Power Electronic Interfaced DG," in *Power Systems Conference and Exposition*, 2006, Atlanta, 2006, pp. 1423−1428.

[8] Y. Liu, C. Farnell, K. George, H. A. Mantooth, J. C. Balda, “A Scaled-Down Microgrid Laboratory Testbed,” in *2015 IEEE Energy Conversion Congress and Exposition (ECCE)*, pp.1184−1189, 20−24 Sept. 2015.

[9] M. F. Farias, P. E. Battaiotto, and M. G. Cendoya, "Wind Farm to Weak-Grid Connection using UPQC custom power device," in *IEEE International Conference on Industrial Technology (ICIT)*, 2010, pp. 1745 –1750.

[10] F. Zhou, G. Joos, and C. Abbey, “Voltage stability in Weak Connection Wind Farms,” in *Proc. IEEE Power Engineering Society General Meeting*, Jun. 2005, vol. 2, pp. 1483 – 1488.

[11] Y. Liu, C. Farnell, J. C. Balda, and H. A. Mantooth, "A 13.8-kV 4.75- MVA microgrid laboratory test bed," in *Proc. IEEE Applied Power Electronics Conference and Exposition (APEC)*, pp. 697–702, Mar. 2014.

[12] "Perform Transformation From Three-Phase (abc) Signal To dq0 Rotating Reference Frame Or The Inverse – Simulink," *Mathworks.com*. N.p., 2016. Web. 30 Mar. 2016.

[13] A.K. Srivastava, A.A. Kumar, and N.N. Schulz, "Impact of the Distributed Generations with Energy Storage on the Electric Grid," in *IEEE Systems Journal*, Vol. 6, no. 1, pp. 110 –117, Mar. 2012.

[14] Y. Shuito, Q. Lei, F. Peng, and Z. Quian, "A robust control scheme for grid-connected voltage-source inverters," in *IEEE Transactions on Indrustrial Electronics*, vol.58, no.1, pp. 202 – 210, Jan. 2011.

[15] A. K. Srivastava, R. Zamora, and D. Bowman, "Impact of Distributed Generation with Storage on Electric Grid Stability," in *Proc. 2011 IEEE Power and Energy Society General Meeting*, pp 1-5 Jul. 2011.

[16] S. S. Refaat, H. Abu-Rub, and A. P. Sanfilippo, "Voltage Stability of Large-Scale Photovoltaic System on Electric Power Grids," in *Renewable Power Generation, 5th IET International Conference*, pp. 1-6, Sep. 2016.

[17] M. Fard and M. Aldeen, "Linear Quadratic Regulator design for a hybrid photovoltaic-battery system," in *2016 Australian Control Conference (AuCC)*, Newcastle, NSW, 2016, pp. 347-352.

[18] C. Y. Tang, Y. F. Chen, Y. M. Chen and Y. Y. Chang, "DC-Link Voltage Control Strategy for Three-Phase Back-to-Back Active Power Conditioners," in *IEEE Transaction on Industry Applications*., vol. 62, no. 10, pp. 6306–6316, Oct. 2015.

[19] B. G. Gu and K. Nam, "A dc-link capacitor minimization method through direct capacitor current control," *IEEE Transaction on Industry Applications*., vol. 42, no. 2, pp. 573–581, Mar./Apr. 2006.

[20] F. Ornelas-Tellez, "Optimal control for a renewable-energy-based micro-grid," in *2014 IEEE International Autumn Meeting on Power, Electronics and Computing (ROPEC)*, Ixtapa, 2014, pp. 1-6.

[21] G. J. Rogers, "Control for stability in interconnected power systems," in *IEEE Control Systems Magazine*, vol. 9, no. 1, pp. 19-22, Jan. 1989.

[22] *Electric Power Systems and Equipment – Voltage Ratings (60 Hertz)*, ANSI Standard C84.1, 2011.

[23] K. Ogata, “Control Systems Design in State Space,” in *Modern Control Engineering*, 5th ed. Upper Saddle River, NJ: Pearson Educ. Ch. 10, sec. 2-9, pp.723 – 806.

[24] Y. Zhu, X. Shi and Y. Dan, "Deduction of coordinate transform for instantaneous reactive power theory and analysis on relationship between α — β and dq0 transformation," in *2009 9th International Conference on Electronic Measurement & Instruments*, Beijing, 2009, pp. 4-922-4-925.

[25] K. Mu, X. Ma, X. Mu and D. Zhu, "A new nonlinear control strategy for three-phase Photovoltaic grid-connected inverter," in *Proceedings of 2011 International Conference on Electronic & Mechanical Engineering and Information Technology*, Harbin, Heilongjiang, 2011, pp. 4611-4614.

[26] National Center for Reliable Power Transmission, [Online]. Available: ncrept.uark.edu

[27] R. Abdulkader, A. Niragire and R. A. McCann, “Sliding mode control for improved stability and disturbance rejection in ring bus conFig. microgrids,” in *49th Annual Frontiers of Power Conference*, Stillwater, OK, 2016, pp. 1-5.

[28] A. Niragire, R. Abdulkader and R. A. McCann, “Linear Quadratic Gaussian Control for Resonance Damping in Microgrids with Cascaded Converters,” in *IEEE PES Innovative Smart Grid Technologies Conferences*, 2017, pp. 1-5.

## APPENDICES

### Appendix A: NCREPT Microgrid System Parameters

Appendix A summarizes the parameters and their values for the microgrid modelled in chapter III.

TABLE A.1
TRANSFORMERS

| Transformer Name | Connection Type | Voltage (kV) | Rated Power (kVA) | Impedance (~ %) |
|---|---|---|---|---|
| T1 | Δ/Y | 0.480/13.8 | 2500 | 5 |
| T2 | Δ/Y | 0.480/13.8 | 2500 | 5 |
| T3 | Δ/Y | 0.480/13.8 | 2500 | 5 |
| T4 | Δ/Y | 0.480/13.8 | 2500 | 5 |
| T5 | Δ/Y | 0.480/13.8 | 2500 | 5 |
| T6 | Δ/Y | 0.480/13.8 | 2500 | 5 |
| Utility Txmr | Y/Y | 12.47/0.480 | 15000 | 5 |

TABLE A.2
REGENERATIVE DRIVE (REGEN) - PARAMETERS

| Name | Unit Value | Set Up | Total Value |
|---|---|---|---|
| EMI Filter Cap | 20 μF | 1 per line, input side | 20 μF |
| Filter Cap | 3 x 96 μF, Δ | 5 on each side | 3 x 480 μF |
| Filter Inductor | 20 μH @ 2500 A | 1 on each side | 20 μH |
| DC Capacitor | 2700 μF | 28 \|\| of series pairs | 37800 μF |
| Rectifier Switching Frq | 4 kHZ | | 4 kHz |
| Inverter Switching Frq. | 5 kHZ | | 5 kHz |

TABLE A.3
VARIABALE VOLTAGE VARIABLE FREQUENCY (VVVF) DRIVE - RATINGS

| Name | Unit Value |
|---|---|
| Input Voltage | 120 - 528 Vac |
| Output Voltage | ---------- |
| Output Current | 2000 A (RMS) @ 30 ºC |
| IGBT Current | 1500 A DC, Continuous |
| Input Frequency | 47-63 Hz |
| Output Frequency | ---------- |
| Overload Capacity | 110 % for 60 sec, 125 % for 3 sec |

TABLE A.4

VARIABALE VOLTAGE VARIABLE FREQUENCY (VVVF) DRIVE - PARAMETERS

| Name | Unit Value | Set Up | Total Value |
|---|---|---|---|
| EMI Filter Cap | 20 μF | 2 per line, on input side only | 40 μF |
| Filter Cap | 3 x 96 μF, Δ | 10 on each side | 3 x 960 μF |
| Filter Inductor | 110 μH @ 750 A | 1 on each side | 110 μF |
| DC Capacitor | 2700 μF | 28 \|\| of series pairs | 37800 μF |
| Rectifier Switching Frq | 8 kHZ | | 8 kHz |
| Inverter Switching Frq | 10 kHZ | | 10 kHz |

TABLE A.5

VARIABALE VOLTAGE VARIABLE FREQUENCY (VVVF) DRIVE - RATINGS

| Name | Unit Value |
|---|---|
| Input Voltage | 360 - 528 Vac |
| Output Voltage | 120 - 520 Vav |
| Output Current | 685 A (RMS) @ 40 ºC |
| IGBT Current | 1500 A DC, Continuous |
| Input Frequency | 47-63 Hz |
| Output Frequency | 45-66 Hz |
| Overload Capacity | 150 % for 60 sec, 175 % for 3 sec |

## Appendix B: Sample Transfer Functions in the Laplace Domain

This appendix provides sample transfer functions for the multiple inputs multiple outputs (MIMO) system designed in chapter V.

$$T_3 = \frac{V_{dc1}(s)}{U_1(s)} =$$

-1.19e05 s^23 - 2.03e13 s^22 - 1.387e21 s^21 - 4.824e28 s^20 - 8.965e35 s^19 - 8.668e42 s^18 - 4.11e49 s^17 - 7.609e55 s^16 - 2.71e60 s^15 - 7.737e64 s^14
- 1.417e69 s^13 - 2.204e73 s^12 - 2.604e77 s^11 - 2.678e81 s^10 - 2.175e85 s^9 - 1.545e89 s^8 - 8.486e92 s^7 - 4.013e96 s^6 - 1.292e100 s^5
- 3.278e103 s^4 - 1.837e106 s^3 + 5.046e109 s^2 + 5.872e112 s + 5.971e114

---

s^24 + 1.773e08 s^23 + 1.282e16 s^22 + 4.848e23 s^21 + 1.03e31 s^20 + 1.243e38 s^19 + 8.433e44 s^18 + 3.003e51 s^17 + 4.41e57 s^16 + 1.928e62 s^15
+ 5.903e66 s^14 + 1.224e71 s^13 + 2.035e75 s^12 + 2.652e79 s^11 + 2.875e83 s^10 + 2.527e87 s^9 + 1.855e91 s^8 + 1.092e95 s^7 + 5.23e98 s^6
+ 1.872e102 s^5 + 4.991e105 s^4 + 7.389e108 s^3 + 5.065e111 s^2 + 1.134e114 s + 7.339e115

$$T_2 = \frac{V_{dc2}(s)}{U_1(s)} =$$

6.614e04 s^23 + 9.247e12 s^22 + 5.008e20 s^21 + 1.328e28 s^20 + 1.83e35 s^19 + 1.35e42 s^18 + 5.074e48 s^17 + 7.715e54 s^16 + 2.577e59 s^15
+ 7.427e63 s^14 + 1.33e68 s^13 + 2.088e72 s^12 + 2.424e76 s^11 + 2.497e80 s^10 + 1.958e84 s^9 + 1.369e88 s^8 + 6.92e91 s^7 + 3.158e95 s^6
+ 8.115e98 s^5 + 2.247e102 s^4 - 3.008e104 s^3 + 1.112e109 s^2 + 1.864e112 s + 2.219e114

---

s^24 + 1.773e08 s^23 + 1.282e16 s^22 + 4.848e23 s^21 + 1.03e31 s^20 + 1.243e38 s^19 + 8.433e44 s^18 + 3.003e51 s^17 + 4.41e57 s^16 + 1.928e62 s^15
+ 5.903e66 s^14 + 1.224e71 s^13 + 2.035e75 s^12 + 2.652e79 s^11 + 2.875e83 s^10 + 2.527e87 s^9 + 1.855e91 s^8 + 1.092e95 s^7 + 5.23e98 s^6
+ 1.872e102 s^5 + 4.991e105 s^4 + 7.389e108 s^3 + 5.065e111 s^2 + 1.134e114 s + 7.339e115

$$T_3 = \frac{V_{dc1}(s)}{U_1(s)} =$$

1.759e11 s^21 + 2.497e19 s^20 + 1.37e27 s^19 + 3.669e34 s^18 + 5.091e41 s^17 + 3.769e48 s^16 + 1.421e55 s^15 + 2.161e61 s^14 + 6.093e65 s^13
- 7.557e70 s^12 - 2.268e75 s^11 - 4.992e79 s^10 - 6.698e83 s^9 - 7.319e87 s^8 - 5.816e91 s^7 - 3.867e95 s^6 - 1.923e99 s^5 - 8.015e102 s^4
- 2.267e106 s^3 - 4.646e109 s^2 + 1.476e112 s + 2.233e114

---

s^24 + 1.773e08 s^23 + 1.282e16 s^22 + 4.848e23 s^21 + 1.03e31 s^20 + 1.243e38 s^19 + 8.433e44 s^18 + 3.003e51 s^17 + 4.41e57 s^16 + 1.928e62 s^15
+ 5.903e66 s^14 + 1.224e71 s^13 + 2.035e75 s^12 + 2.652e79 s^11 + 2.875e83 s^10 + 2.527e87 s^9 + 1.855e91 s^8 + 1.092e95 s^7 + 5.23e98 s^6
+ 1.872e102 s^5 + 4.991e105 s^4 + 7.389e108 s^3 + 5.065e111 s^2 + 1.134e114 s + 7.339e115

## Appendix C: Actual Model Measured States before Applying a Low Pass Filter

This appendix provides raw data by means of graphs for actual circuit model for the model comparison results presented in chapter III.

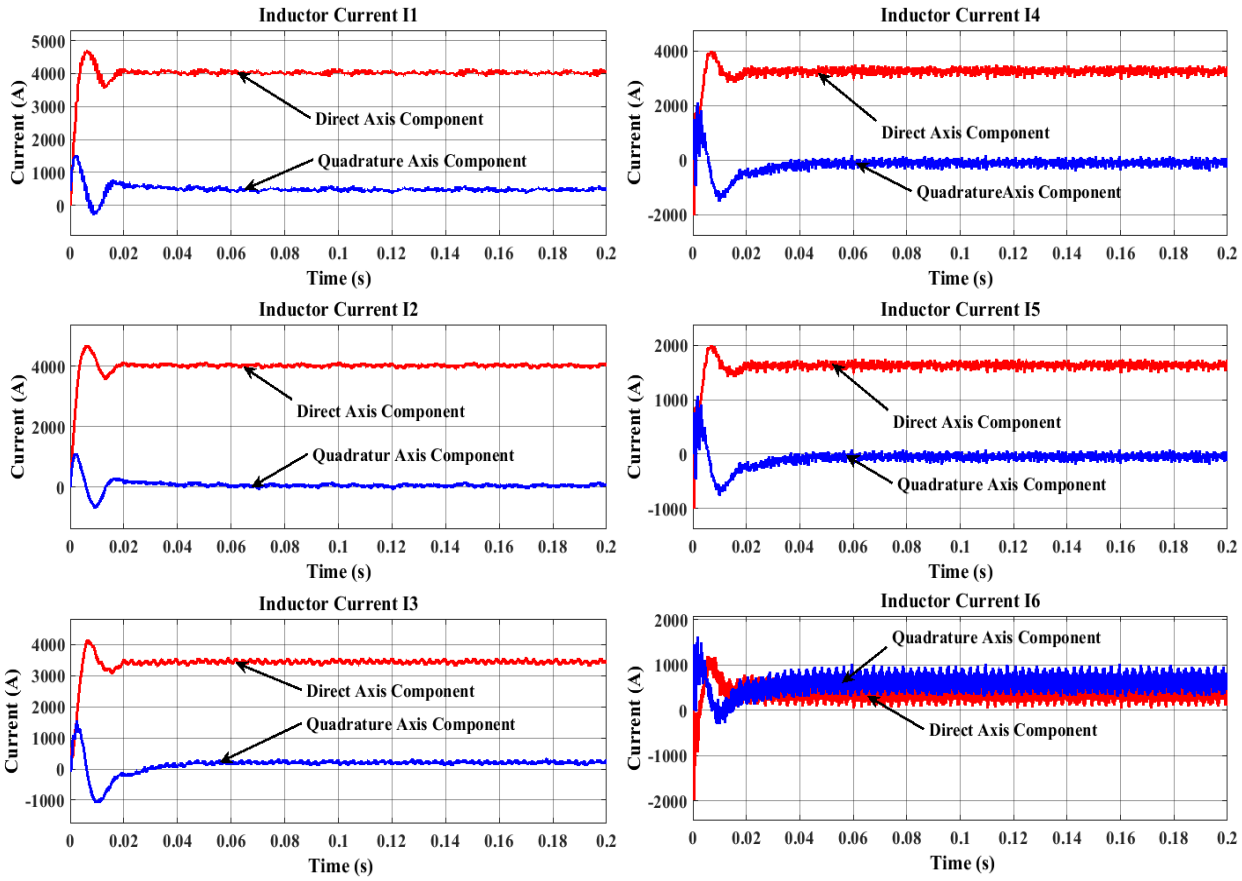


Fig. C. 1. Inductor currents for the actual model.

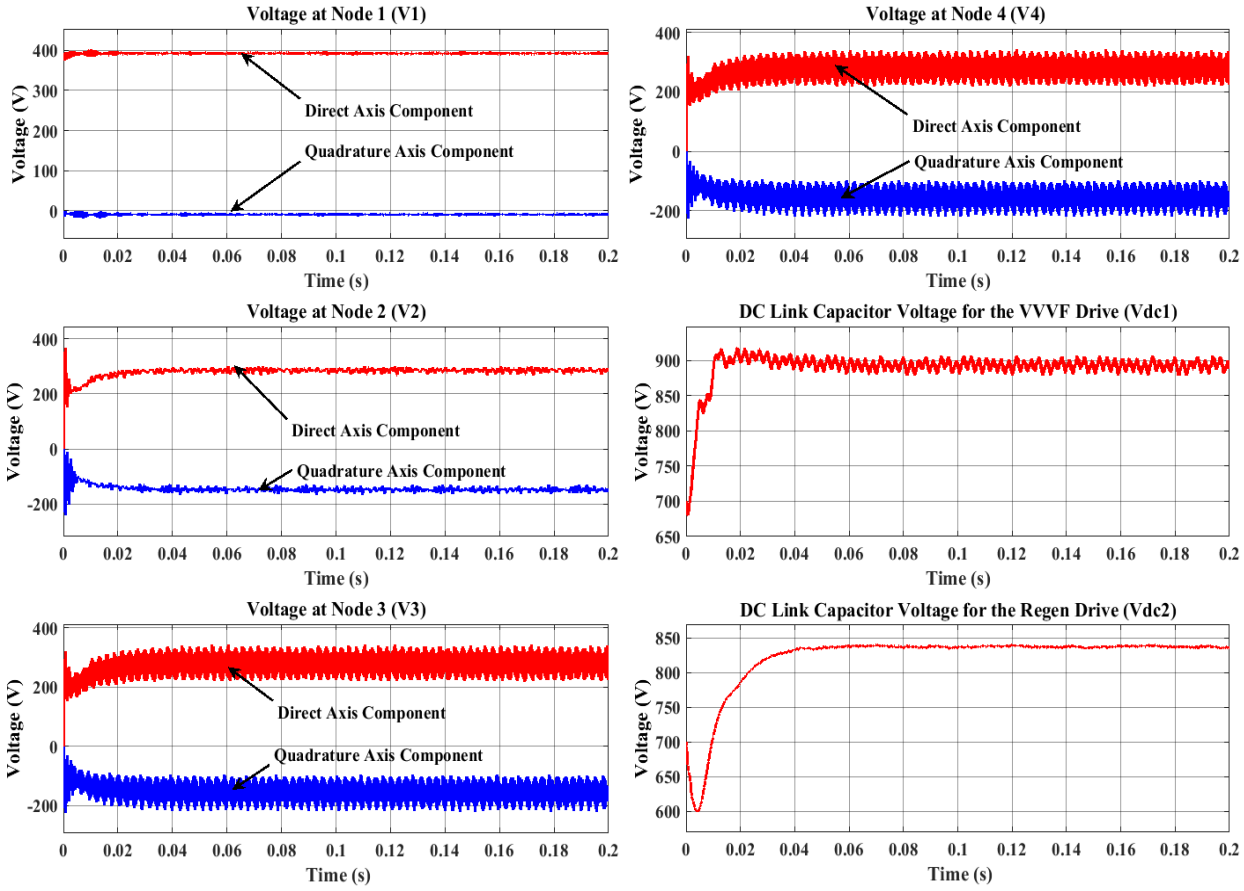


Fig. C. 2. Capacitor Voltages for the actual model.

## Appendix D: Mathematical Model Measured States before Applying a Low Pass Filter

This appendix provides raw data by means of graphs for linearized mathematical model for the model comparison results presented in chapter III.

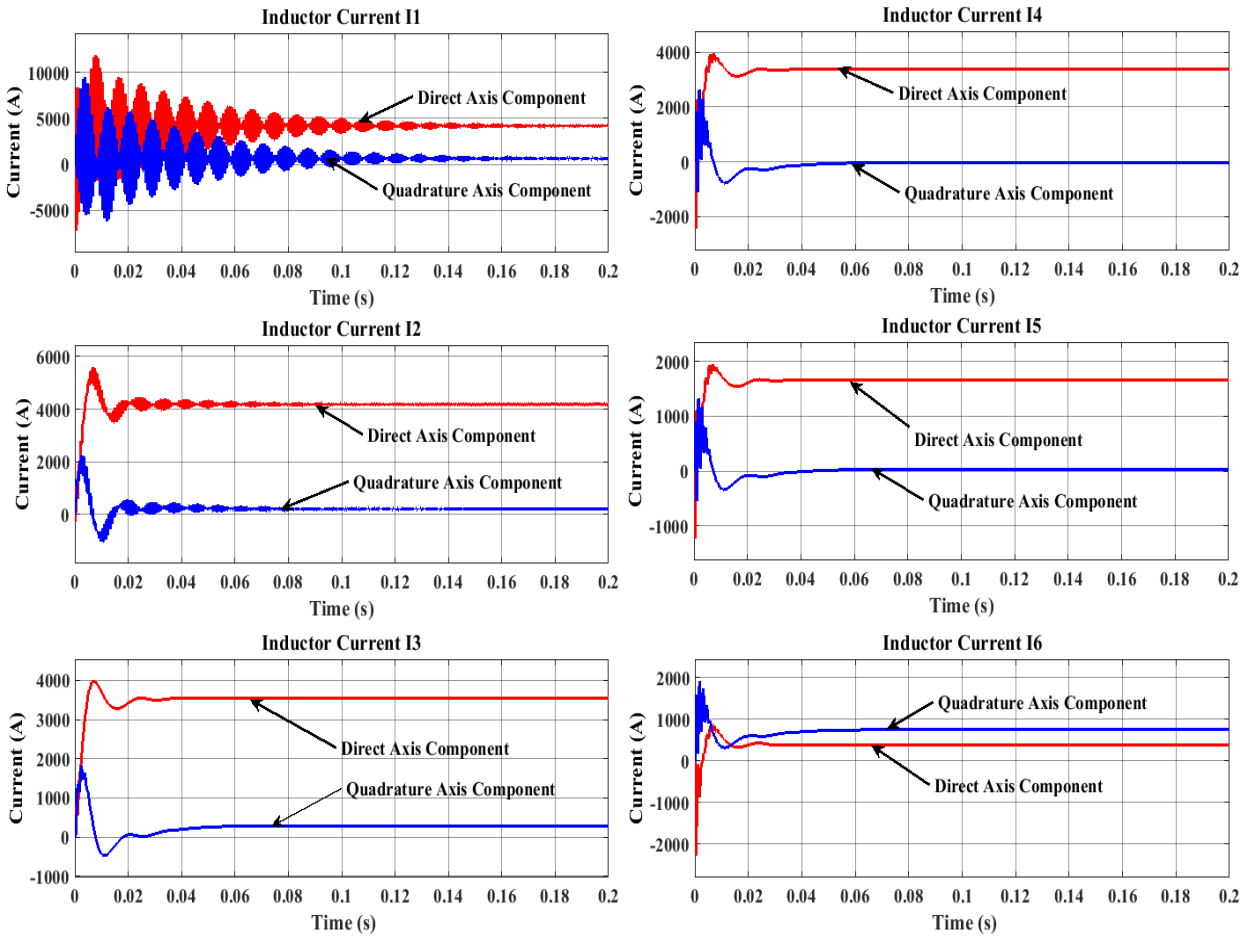


Fig. C. 2. Inductor Currents for the actual model.

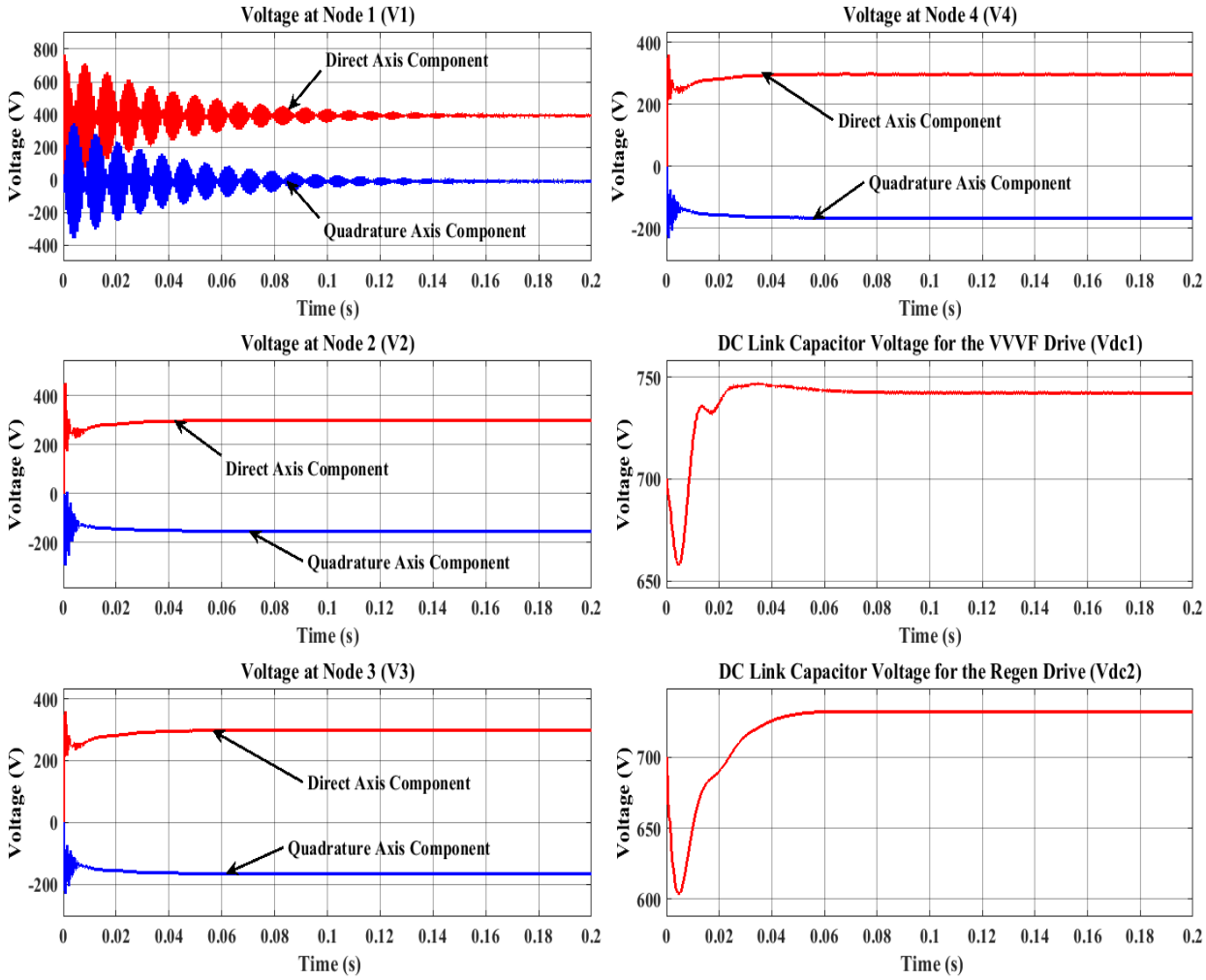


Fig. C. 2. Capacitor Voltages for the actual model.

## Appendix E: Controller Performance Evaluation – Supplemental Data

This appendix shows how the controller performance characteristics presented in chapter V were measured using Matlab/Simulink™.

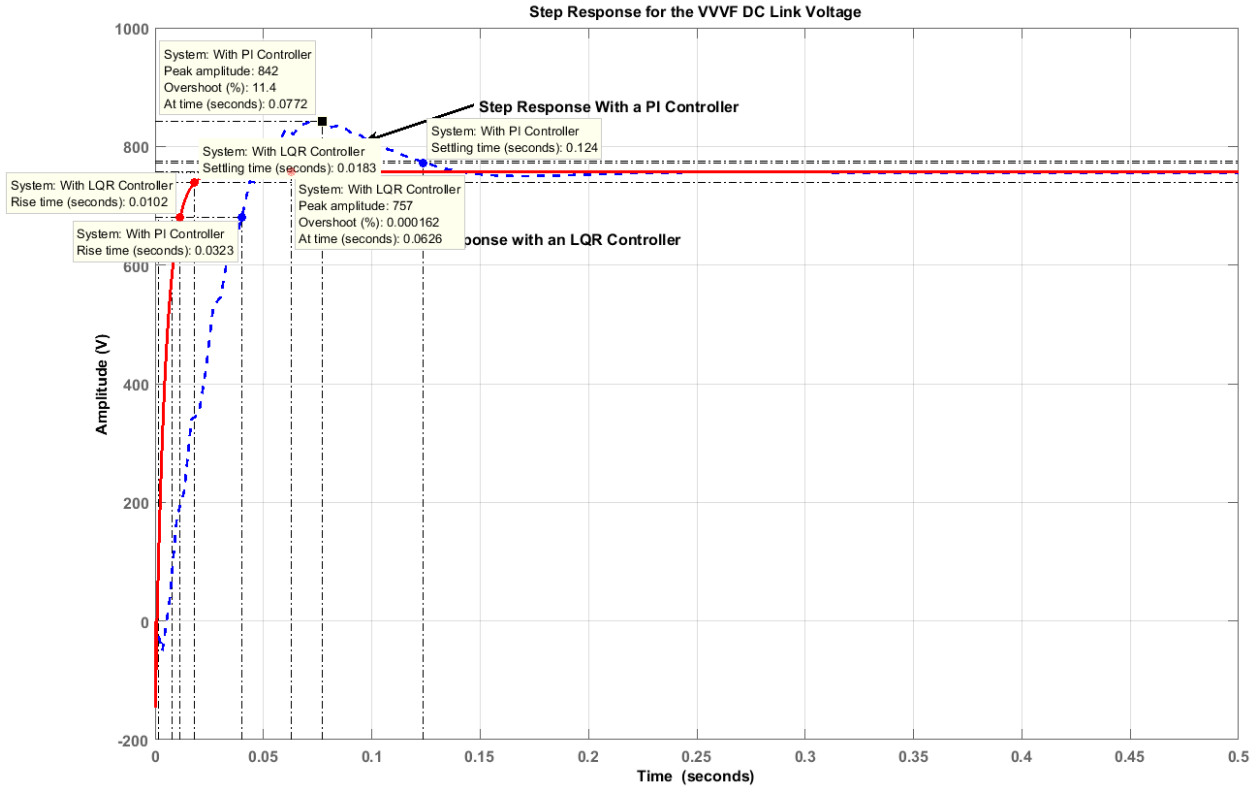

**Appendix F: System Matrix for the Linearized Mathematical Model**

Appendix F gives the explicit system matrices for the linearized model, which was derived in chapter III.

$\overline{A} = \frac{\partial f}{\partial x}\Big|_{(\bar{x},\bar{u})} = \begin{bmatrix} \overline{A}_{11} & \overline{A}_{12} \\ \overline{A}_{21} & \overline{A}_{22} \end{bmatrix}$ where:

$$\overline{A}_{11} = \begin{bmatrix}
-\frac{R_T}{L_T} & \omega & 0 & 0 & 0 & 0 & 0 & 0 & 0 & 0 & 0 & 0 \\
-\omega & -\frac{R_T}{L_T} & 0 & 0 & 0 & 0 & 0 & 0 & 0 & 0 & 0 & 0 \\
0 & 0 & -\frac{R_1}{L_1} & \omega & 0 & 0 & 0 & 0 & 0 & 0 & 0 & 0 \\
0 & 0 & -\omega & -\frac{R_1}{L_1} & 0 & 0 & 0 & 0 & 0 & 0 & 0 & 0 \\
0 & 0 & 0 & 0 & -\frac{R_2}{L_2} & \omega & 0 & 0 & 0 & 0 & 0 & 0 \\
0 & 0 & 0 & 0 & -\omega & -\frac{R_2}{L_2} & 0 & 0 & 0 & 0 & 0 & 0 \\
0 & 0 & 0 & 0 & 0 & 0 & -\frac{R}{L} & \omega & 0 & 0 & 0 & 0 \\
0 & 0 & 0 & 0 & 0 & 0 & -\omega & -\frac{R}{L} & 0 & 0 & 0 & 0 \\
0 & 0 & 0 & 0 & 0 & 0 & 0 & 0 & -\frac{R}{L} & \omega & 0 & 0 \\
0 & 0 & 0 & 0 & 0 & 0 & 0 & 0 & -\omega & -\frac{R}{L} & 0 & 0 \\
0 & 0 & 0 & 0 & 0 & 0 & 0 & 0 & 0 & 0 & -\frac{R_3}{L_3} & \omega \\
0 & 0 & 0 & 0 & 0 & 0 & 0 & 0 & 0 & 0 & -\omega & -\frac{R_3}{L_3}
\end{bmatrix}$$

$$\bar{A}_{12} = \begin{bmatrix} 0 & 0 & 0 & 0 & -\frac{1}{L_T} & 0 & 0 & 0 & 0 & 0 & 0 & 0 \\ 0 & 0 & 0 & 0 & 0 & -\frac{1}{L_T} & 0 & 0 & 0 & 0 & 0 & 0 \\ 0 & 0 & -\frac{\bar{\mu}_{1d}}{L_1} & 0 & \frac{1}{L_1} & 0 & 0 & 0 & 0 & 0 & 0 & 0 \\ 0 & 0 & -\frac{\bar{\mu}_{1q}}{L_1} & 0 & 0 & \frac{1}{L_1} & 0 & 0 & 0 & 0 & 0 & 0 \\ 0 & 0 & \frac{\bar{\mu}_{2d}}{L_1} & 0 & 0 & 0 & -\frac{1}{L_2} & 0 & 0 & 0 & 0 & 0 \\ 0 & 0 & \frac{\bar{\mu}_{2q}}{L_1} & 0 & 0 & 0 & 0 & -\frac{1}{L_2} & 0 & 0 & 0 & 0 \\ 0 & 0 & 0 & 0 & 0 & 0 & \frac{2}{3L} & 0 & -\frac{1}{3L} & 0 & -\frac{1}{3L} & 0 \\ 0 & 0 & 0 & 0 & 0 & 0 & 0 & \frac{2}{3L} & 0 & -\frac{1}{3L} & 0 & -\frac{1}{3L} \\ 0 & 0 & 0 & 0 & 0 & 0 & \frac{1}{3L} & 0 & -\frac{2}{3L} & 0 & \frac{1}{3L} & 0 \\ 0 & 0 & 0 & 0 & 0 & 0 & 0 & \frac{1}{3L} & 0 & -\frac{2}{3L} & 0 & \frac{1}{3L} \\ 0 & 0 & 0 & -\frac{\bar{\mu}_{3d}}{L_3} & 0 & 0 & 0 & 0 & \frac{1}{L_3} & 0 & 0 & 0 \\ 0 & 0 & 0 & -\frac{\bar{\mu}_{3q}}{L_3} & 0 & 0 & 0 & 0 & 0 & \frac{1}{L_3} & 0 & 0 \end{bmatrix}$$

$\bar{A}_{22}$

$$=\begin{bmatrix}
-\frac{R_4}{L_4} & \omega & 0 & -\frac{\bar{\mu}_{4d}}{L_4} & 0 & 0 & 0 & 0 & 0 & 0 & \frac{1}{L_4} & 0 \\
-\omega & -\frac{R_4}{L_4} & 0 & -\frac{\bar{\mu}_{4q}}{L_4} & 0 & 0 & 0 & 0 & 0 & 0 & 0 & \frac{1}{L_4} \\
0 & 0 & 0 & 0 & 0 & 0 & 0 & 0 & 0 & 0 & 0 & 0 \\
\frac{\bar{\mu}_{4d}}{C_{DC2}} & \frac{\bar{\mu}_{4q}}{C_{DC2}} & 0 & 0 & 0 & 0 & 0 & 0 & 0 & 0 & 0 & 0 \\
0 & 0 & 0 & 0 & 0 & \omega & 0 & 0 & 0 & 0 & 0 & 0 \\
0 & 0 & 0 & 0 & -\omega & 0 & 0 & 0 & 0 & 0 & 0 & 0 \\
0 & 0 & 0 & 0 & 0 & 0 & 0 & \omega & 0 & 0 & 0 & 0 \\
0 & 0 & 0 & 0 & 0 & 0 & -\omega & 0 & 0 & 0 & 0 & 0 \\
0 & 0 & 0 & 0 & 0 & 0 & 0 & 0 & -\frac{1}{R_{L1}C_3} & \omega & 0 & 0 \\
0 & 0 & 0 & 0 & 0 & 0 & 0 & 0 & -\omega & -\frac{1}{R_{L1}C_3} & 0 & 0 \\
-\frac{1}{C_4} & 0 & 0 & 0 & 0 & 0 & 0 & 0 & 0 & 0 & -\frac{1}{R_{L2}C_4} & \omega \\
0 & -\frac{1}{C_4} & 0 & 0 & 0 & 0 & 0 & 0 & 0 & 0 & -\omega & -\frac{1}{R_{L2}C_4}
\end{bmatrix}$$

$\bar{B} = \left.\frac{\partial f}{\partial u}\right|_{(\bar{x},\bar{u},\bar{u}_d)} = \begin{bmatrix}\bar{B}_{11}\\ \bar{B}_{21}\end{bmatrix}$ with:

$$\bar{B}_{11} = \begin{bmatrix}
0 & 0 & 0 & 0 & 0 & 0 & 0 & 0\\
0 & 0 & 0 & 0 & 0 & 0 & 0 & 0\\
-\frac{\bar{v}_{DC1}}{L_1} & 0 & 0 & 0 & 0 & 0 & 0 & 0\\
0 & -\frac{\bar{v}_{DC1}}{L_1} & 0 & 0 & 0 & 0 & 0 & 0\\
0 & 0 & \frac{\bar{v}_{DC1}}{L_2} & 0 & 0 & 0 & 0 & 0\\
0 & 0 & 0 & \frac{\bar{v}_{DC1}}{L_2} & 0 & 0 & 0 & 0\\
0 & 0 & 0 & 0 & 0 & 0 & 0 & 0\\
0 & 0 & 0 & 0 & 0 & 0 & 0 & 0\\
0 & 0 & 0 & 0 & 0 & 0 & 0 & 0\\
0 & 0 & 0 & 0 & 0 & 0 & 0 & 0\\
0 & 0 & 0 & 0 & -\frac{\bar{v}_{DC2}}{L_3} & 0 & 0 & 0\\
0 & 0 & 0 & 0 & 0 & -\frac{\bar{v}_{DC2}}{L_3} & 0 & 0
\end{bmatrix}$$

$$\bar{B}_{21} = \begin{bmatrix}
0 & 0 & 0 & 0 & 0 & 0 & -\frac{\bar{v}_{DC2}}{L_4} & 0\\
0 & 0 & 0 & 0 & 0 & 0 & 0 & -\frac{\bar{v}_{DC2}}{L_4}\\
\frac{\bar{\imath}_{2d}}{C_{DC1}} & \frac{\bar{\imath}_{2q}}{C_{DC1}} & -\frac{\bar{\imath}_{3d}}{C_{DC1}} & -\frac{\bar{\imath}_{3q}}{C_{DC1}} & 0 & 0 & 0 & 0\\
0 & 0 & 0 & 0 & \frac{\bar{\imath}_{6d}}{C_{DC2}} & \frac{\bar{\imath}_{6q}}{C_{DC2}} & \frac{\bar{\imath}_{7d}}{C_{DC2}} & \frac{\bar{\imath}_{7q}}{C_{DC2}}\\
0 & 0 & 0 & 0 & 0 & 0 & 0 & 0\\
0 & 0 & 0 & 0 & 0 & 0 & 0 & 0\\
0 & 0 & 0 & 0 & 0 & 0 & 0 & 0\\
0 & 0 & 0 & 0 & 0 & 0 & 0 & 0\\
0 & 0 & 0 & 0 & 0 & 0 & 0 & 0\\
0 & 0 & 0 & 0 & 0 & 0 & 0 & 0\\
0 & 0 & 0 & 0 & 0 & 0 & 0 & 0
\end{bmatrix}$$

$$\bar{F} = \left.\frac{\partial f}{\partial u_d}\right|_{(\bar{x},\bar{u},\bar{u}_d)}$$

$$= \begin{bmatrix} \frac{1}{L_T} & 0 & 0 & 0 & 0 & 0 & 0 & 0 & 0 & 0 & 0 & 0 & 0 & 0 & 0 & 0 & 0 & 0 & 0 & 0 & 0 & 0 & 0 & 0 \\ 0 & \frac{1}{L_T} & 0 & 0 & 0 & 0 & 0 & 0 & 0 & 0 & 0 & 0 & 0 & 0 & 0 & 0 & 0 & 0 & 0 & 0 & 0 & 0 & 0 & 0 \\ 0 & 0 & 0 & 0 & 0 & 0 & 0 & 0 & 0 & 0 & 0 & 0 & 0 & 0 & 0 & 0 & 0 & 0 & 0 & 0 & 0 & 0 & \frac{1}{C_4} & 0 \\ 0 & 0 & 0 & 0 & 0 & 0 & 0 & 0 & 0 & 0 & 0 & 0 & 0 & 0 & 0 & 0 & 0 & 0 & 0 & 0 & 0 & 0 & 0 & \frac{1}{C_4} \end{bmatrix}^T$$

The state variable, input and disturbance matrices are given below.

$\mathbf{x} = [i_{1d} \quad i_{1q} \quad . \quad . \quad . \quad i_{7d} \quad i_{7d} \quad v_{CDC1} \quad v_{CDC2} \quad v_{1d} \quad v_{1q} \quad . \quad . \quad . \quad v_{4d} \quad v_{4q}]^T$,

$\mathbf{u} = [\mu_{1d} \quad \mu_{1q} \quad \mu_{2d} \quad \mu_{2q} \quad \mu_{3d} \quad \mu_{3q} \quad \mu_{4d} \quad \mu_{4q}]^T$, and $\mathbf{u_d} = [v_d \quad v_d \quad i_{PVd} \quad i_{PVq}]^\mathbf{T}$.